GEORG-AUGUST-UNIVERSITÄT
GÖTTINGEN

MAX-PLANCK-GESELLSCHAFT

Bachelorarbeit am Max-Planck-Institut Göttingen

Abt. Dynamik komplexer Fluide

Modellierung von *Chlamydomonas reinhardtii* Motilität in geschlossenen Geometrien

Modeling of *Chlamydomonas reinhardtii* motility in confinement

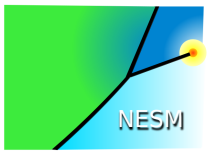

Jan Cammann

jan.cammann@stud.uni-goettingen.de

Erstgutachter:	Dr. Marco G. Mazza MPI für Dynamik und Selbstorganisation Göttingen Dynamik komplexer Fluide
Zweitgutachterin:	Prof. Annette Zippelius Georg-August-Universität Göttingen Institut für Theoretische Physik
Datum:	02. Dezember 2016

Contents

Abstract

Microswimmers, such as bacteria or motile algae, which typically live in water and soil encounter boundaries very frequently. A wide range of different microswimmers seem to spend a significant amount of time close to such boundaries as opposed to staying in the bulk. Different physical mechanisms have been proposed to explain these observations, such as hydrodynamic interactions or steric forces. While hydrodynamics are able to give a good explanation for pusher-type swimmers, its predictions for puller-type swimmers do not explain the trapping at walls. Here the "wall-hugging" effect of puller-type swimmers will be explained. A simple dumbbell model for the cell's shape will be introduced to model the steric wall interactions of *Chlamydomonas reinhardtii* in a quasi 2d environment. Simulations of this model will be performed and compared with experimental results.

1 Introduction

1.1 Active Brownian particles

Particles within a fluid experience collisions with the randomly moving molecules of the fluid. These collisions lead to a random movement of the particle which is called Brownian motion. Einstein was the first to theoretically describe this phenomenon [1]. While the concept of Brownian motion itself is very well studied, active Brownian particles have lately been the subject of many publications [2–4]. In contrast to passive ones, active Brownian particles do not just stay in thermodynamic equilibrium with their surroundings. By definition they possess the ability to inject energy into the system making them an interesting subject of nonequilibrium physics [5].

Microorganisms living in an aqueous environment, whether they are bacteria like *E. coli*, algae like *Chlamydomonas reinhardtii* or spermatozoa, that do not rely on thermal fluctuations for their movement and instead have the additional ability to propel themselves forward are classified as microswimmers. In addition to the biological ones, there are efforts to create artificial microswimmers for various purposes, like localizing and transporting nanoscopic objects for targeted drug delivery or gene therapy [6, 7].

The ability of self-propulsion leads to a mixture of aimed movement and the random walk of passive Brownian motion. This behavior drives them out of thermodynamic equilibrium with their surroundings [8]. While passive Brownian particles follow the fluctuation-dissipation theorem and thereby the Stokes-Einstein relation $D = \frac{k_B T}{\gamma}$, this relation no longer holds true for active particles [9].

1.2 *Chlamydomonas reinhardtii*

Chlamydomonas reinhardtii is a unicellular alga found worldwide mainly in soil and fresh water. It is quite easy to grow in labs and comparably easy to handle and characterize its mutants. Additionally, the complete *Chlamydomonas* genome has been sequenced [10]. Therefore, it has served as a model organism for many studies concerning microorganisms over the last years [5]. It has two flagella attached to the "front" of its spherical cell body. When the cell swims they beat in a breaststroke-like pattern at $\sim$ 50Hz. This behavior makes the cells movement fundamentally different from other microswimmers that have their flagella attached at their rear end like spermatozoa or *E. coli* which will be discussed in more detail in section 2.1.2. *Chlamydomonas* flagella have a length of $\sim 10 - 12\mu$m [5] which is roughly twice as long as the cell's body. When studying their movement it is important to

keep in mind that they possess an eyespot, giving them the ability to sense light and perform phototaxis. Additionally, their center of mass is displaced towards their rear end, so a gyrotactic torque acting on them induces a tendency to swim upward [5].

In addition to its breaststroke *Chlamydomonas* has the ability to perform a second kind of motion called 'gliding', where the cell's flagella adhere to a boundary and the cell crawls along it. This movement typically lasts for a couple of seconds and leads to velocities of $\sim 1.5\mu\mathrm{m\,s}^{-1}$ [5] which is considerably slower than their swimming speed, which is about $60\mu\mathrm{m\,s}^{-1}$ [11].

1.3 Wall interactions of microswimmers

On its way through a medium a microswimmer is likely to encounter different kinds of boundaries, e.g. liquid-liquid or liquid-gas interfaces, cell membranes or solid walls. *Chlamydomonas*, for examples, can be found in soil [5], so their habitat is filled with boundaries of different geometries. A great variety of microswimmers seems to accumulate at such boundaries [12]. This behavior is explained with a variety of effects, like van der Waals forces, hydrodynamics, and steric forces [12, 13]. Which effect is dominant seems to vary for different swimmers and environments. While hydrodynamic interactions can change the speed and trajectories of swimmers near a wall, they mainly depend on the mechanism the swimmer uses for propulsion [12]. This will be illuminated further in section 2.1.2. Steric forces on the other hand mostly depend on the swimmer's shape and softness as well as wall curvature [11]. The shape of the microswimmer is often just modeled as a rod or a simple sphere [13]. Since microswimmers are of a more complex shape a different and more refined model, which comes closer to the actual stroke-averaged shape of *Chlamydomonas*, will be introduced in section 2.2.2.

2 Theoretical basics

2.1 Microswimmer hydrodynamics

To understand the swimming strategies of microswimmers and hence the equations of motion used to model the swimmer trajectories it is important to get an understanding of the environment they live in [12, 14]. Swimming on a microscopic scale is vastly different from what humans usually think of when they talk about swimming.

2.1.1 Low Reynolds number hydrodynamics

For incompressible Newtonian fluids, such as water, hydrodynamic flows follow the Navier-Stokes equations [12]

$$\begin{aligned} \rho\left(\frac{\partial}{\partial t}+\boldsymbol{u}\cdot\nabla\right)\boldsymbol{u} &= -\nabla p+\eta\nabla^2\boldsymbol{u}, \\ \nabla\cdot\boldsymbol{u} &= 0, \end{aligned} \tag{1}$$

where ρ is the density, $\boldsymbol{u}$ the convective velocity, p the hydrostatic pressure, and η the viscosity of the fluid. The first equation represents the conservation of momentum in the fluid, and the second one the condition of incompressibility.

To nondimensionalize the Navier-Stokes equations (1) the Reynolds number $\mathcal{R}=\rho UL/\eta$ [12] is commonly used. U and L are the characteristic velocity and length scales of the flow. One possible interpretations of the Reynolds number is the ratio of inertial to viscous forces $\mathcal{R}=f_{\text{inertial}}/f_{\text{viscous}}$ [12], so that processes happening at low $\mathcal{R}$ are dominated by viscous drag forces, while inertia plays little to no role. Macroscopic creatures, such as humans, usually operate at larger Reynolds numbers, where it is preferable to utilize inertia to keep moving. At Reynolds numbers close to zero inertia is not important due to the large viscous damping. Therefore microorganisms have developed swimming strategies quite different to overcome drag.

For the organisms we are going to consider here the Reynolds number usually is around 10^{-4} down to 10^{-5} [14]. Thus, it is appropriate to consider the limit $\mathcal{R}\to 0$ where one can neglect the inertia terms in equation (1), which leads to the so called Stokes equations [12]

$$\begin{aligned} -\nabla p+\eta\nabla^2\boldsymbol{u} &= 0 \\ \nabla\cdot\boldsymbol{u} &= 0. \end{aligned} \tag{2}$$

These equations are linear and time independent. That implies that microswimmers will travel the same distance with one stroke whether they perform it fast or slow. There is even the possibility to perform movements in reverse to exactly reverse the trajectory. A micro-scallop for example, closing fast and then slowly reversing its motion would not have any net displacement away from its initial position at such conditions [12, 14].

2.1.2 Hydrodynamic interactions at low Reynolds numbers

Although there are many possible forms of non-reciprocal motion that would lead to movement, it seems that most biological microswimmers use slender appendages to generate thrust. There are a few exceptions to that like *Spiroplasma*, which is helically shaped and swims by propagating kinks along its body [15]. The number and length of appendages can vary from just one long flagellum, like sperm has, to thousands of short cilia covering the swimmer's surface following a beating pattern, like *Paramecium* [16]. Flagella can be used in different ways such as the rotating helix of *E. coli* [17], whip-like motions of spermatozoa or the breaststroke like patterns of *Chlamydomonas* [18].

Apart from steric wall interactions, that will be described in section 2.2.3, microswimmers also interact with walls through hydrodynamics. Since solutions of the Stokes equation (2) can be approximated using a multipole expansion, similar to the electric field in electrostatics, the method of image charges from electrostatics can be carried over to low Reynolds number hydrodynamics. The point charge analogue here is called a Stokeslet [12]. It represents a flow field produced by a point force acting upon the fluid. Since we can effectively fulfill the no-slip condition at a wall by superposition of the flow fields of two swimmers on either side of the wall studying hydrodynamic swimmer-swimmer interactions will also give an idea of how swimmers will behave near a wall.

Since the system as a whole has to be force free, the easiest approximation of a microswimmer has to be a force dipole, that is two equal and opposite point forces. Swimmers with a body elongated along their swimming direction can typically be categorized into two different types, determined by the force dipole needed to describe them. This dipole typically points in the swimming direction and can either have positive or negative sign, which classifies the swimmer as a 'pusher' or a 'puller', respectively [12]. Prototypical 'pushers' are for example spermatozoa or *E. coli*, which repel fluid from their front and back and draw fluid in to their sides (figure 1a). *Chlamydomonas* pull in fluid from their front and back, while pushing it out from their sides. This makes them an example for 'pullers'. The flow induced

by a pure force dipole $\boldsymbol{p} = p\hat{\boldsymbol{e}}$ reads

$$\boldsymbol{u}(\boldsymbol{r}) = \frac{p\boldsymbol{r}}{8\pi\mu r^3}\left(3\cos^2(\theta) - 1\right), \tag{3}$$

where θ denotes the angle between the dipole $\boldsymbol{p}$ and position $\boldsymbol{r}$ [12]. Plugging $\theta = \pi/2$ into that equation yields the velocity two identical swimmers experience, when swimming side by side, namely $\boldsymbol{u}(\theta = \pi/2) = -p\boldsymbol{r}/8\pi\mu r^3$. This velocity makes pushers attract each other when swimming next to each other, while pullers get repelled. Taking the curl of the velocity field in equation (3) [12]

$$\nabla \times \boldsymbol{u} = \frac{3p}{4\pi\nu}\frac{(\boldsymbol{e}\cdot\boldsymbol{r})(\boldsymbol{e}\times\boldsymbol{r})}{r^5} \tag{4}$$

gives insight into the behavior of microswimmers when approaching each other. Spherical swimmers would rotate at a rate $\Omega_{\text{sphere}} = \frac{1}{2}(\nabla \times \boldsymbol{u})$ [19]. Additionally, flattened or elongated spheroids will align with the principal axis of strain with $\Omega_2 \propto \boldsymbol{e} \times (\boldsymbol{E}\cdot\boldsymbol{e})$, where $\boldsymbol{E}$ is the rate of strain $\boldsymbol{E} = \frac{1}{2}\left(\nabla\boldsymbol{u} + \nabla\boldsymbol{u}^T\right)$. Ω_2 has positive sign for prolate spheroids and negative sign for oblate ones. Since $\boldsymbol{E}$ and $\nabla \times \boldsymbol{u}$ change their sign with p, different rotational behavior for pushers and pullers has to be expected. Two converging pushers for example will align parallel to each other, while pullers will align antiparalell (see figure 1c and 1d).

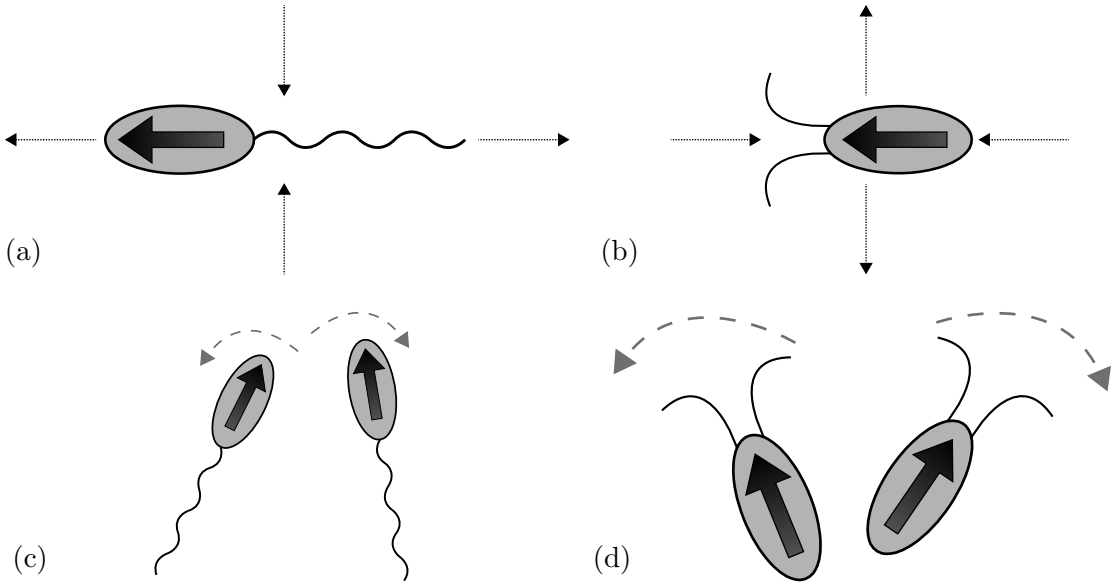

Figure 1: Schematic representation of the flow fields created by pushers with a positive force dipole (a) and pullers with a negative one (b), and hydrodynamic cell cell interactions for pushers aligning parallel to each other (d) and pullers aligning antiparallel (c) when approaching. The large black arrows represent the swimming direction.

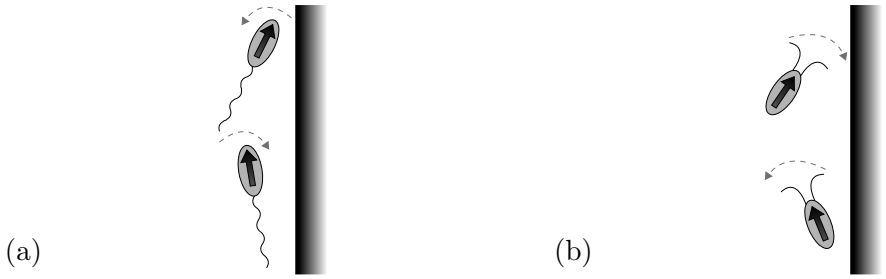

Figure 2: Rotation of microswimmers induced by a nearby wall for pushers (a) and pullers (b).

Analogously, swimmers at flat boundaries experience the force and torque of their mirror image, leading to the fact that swimmers near walls will show the same behavior and will align parallel (figure 2a) or antiparallel (figure 2b) to walls. Additionally, boundaries can have another effect on some swimmers, especially the ones using helical flagella for propulsion. When swimming freely the force applied by the flagellum is parallel to the swimming direction when averaged over one period of the helix rotation, but there are still perpendicular forces that average out over time. Close to walls there is a coupling between the forces applied from the flagellum in direction of the wall and the cells body, leading to a net torque on the cell [12]. Swimmers experiencing this effect tend to swim in circles near boundaries.

2.2 Modeling microswimmers

2.2.1 The Langevin equation

An active Brownian particle, as described in section 1.1, that uses its energy to swim at a constant speed v_0 in direction $\boldsymbol{e}$ is a simple model for a microswimmer. We assume overdamped dynamics, meaning that $\mathcal{R} \to 0$ from which follows that $f_{\text{inertial}} \ll f_{\text{viscous}}$ (see section 2.1.1). Furthermore, the inertial terms $m\ddot{\boldsymbol{r}}$ in the Newtonian equation of motion can be dropped, leaving a first order differential equation [20] which is sufficient to describe the swimmer's motion. The result is a Langevin equation

$$\frac{\mathrm{d}\boldsymbol{r}}{\mathrm{d}t} = v_0 \boldsymbol{e}(t) + \boldsymbol{\eta}, \tag{5}$$

where $\boldsymbol{\eta}$ is a Gaussian white-noise vector with zero mean representing the variations in the swimmers velocity, and with correlation $\langle \boldsymbol{\eta}(t)\boldsymbol{\eta}(t')\rangle = 2k_{\mathrm{B}}T\gamma_w \mathbf{1}\delta(t-t')$, where $\delta(t)$ is the Dirac delta distribution [13]. The orientation of the swimmer then evolves

according to

$$\frac{\mathrm{d}\boldsymbol{e}}{\mathrm{d}t} = \boldsymbol{\xi} \times \boldsymbol{e}, \tag{6}$$

where $\boldsymbol{\xi}$ is a Gaussian white-noise vector with zero mean and $\langle \boldsymbol{\xi}(t)\boldsymbol{\xi}(t')\rangle = \frac{2k_\mathrm{B}T}{\tau_p}\mathbf{1}\delta(t-t')$, modeling variations in the swimmers orientation [13].

2.2.2 Modeling *Chlamydomonas*

A *Chlamydomonas* cell is modeled as an asymmetric dumbbell consisting of two spheres, inspired by the model used by Wysocki *et al.* [13]. One sphere represents the stroke-averaged shape of the cell's flagella with radius $a_1 = 5\mu$m, and the other one represents the cell's body with radius $a_2 = 2.5\mu$m. These sizes correspond to the actual dimensions of *Chlamydomonas*. The two spheres are separated by a fixed distance $l = 5\mu$m. The swimming direction $\boldsymbol{e}$ points from the center of the second sphere towards the first sphere. A graphical representation of this model can be seen in figure 3(a). A dumbbell model is chosen because it is the simplest model which will experience a torque due to steric interactions with the wall. Notice that this is not the case for a simple sphere.

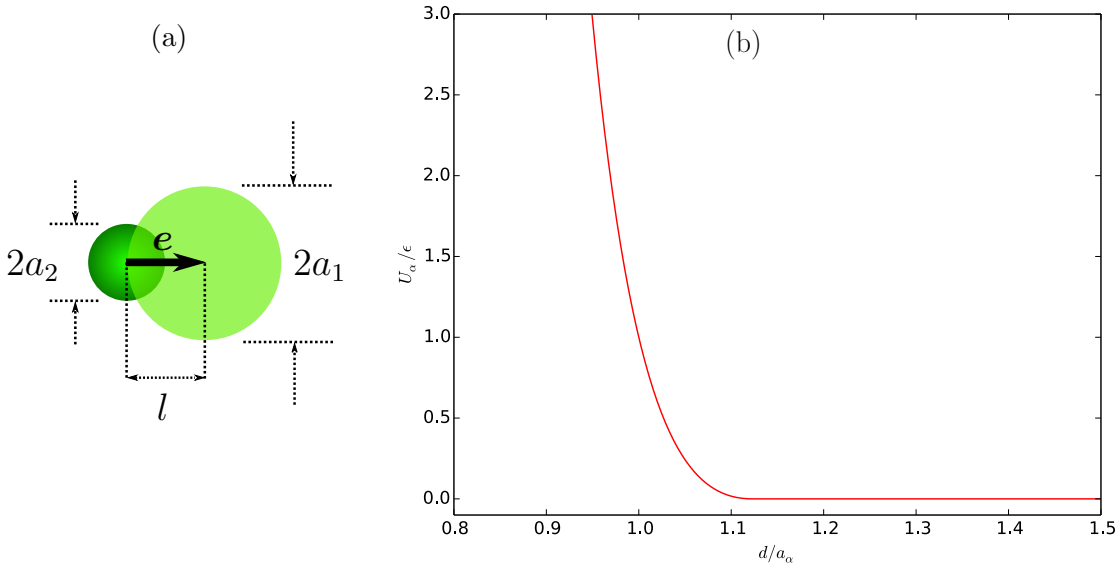

Figure 3: (a) Asymmetric dumbbell modeling a *Chlamydomonas* cell for steric wall interactions consisting of a small sphere of radius a_2 for the cell's body and a larger sphere of radius a_1 representing the stroke-averaged shape of the cell's flagella [11]. (b) Plot of the WCA potential used to model a hard wall.

Similar models to the one described above have been used before to understand steric interactions with walls. Wysocki *et al.* [13] varied the radii a_1 and a_2 and

determined the mean time τ a swimmer stays at the wall as a function of the swimmer's persistence length. They found fundamentally different behavior for polar (meaning $a_1 < a_2$) and antipolar ($a_1 > a_2$) swimmers, like *Chlamydomonas*. For short persistence lengths they found that the trapping times are quite similar for polar and antipolar swimmers, since the turning frequency is very high. For larger persistence lengths however polar swimmers get trapped for really long times, since they continuously bump into the wall (see figure 4b). Antipolar swimmers align with the wall with an angle θ making their swimming direction pointing slightly away from the wall, making them escape much faster (see figure 4a). The angle θ is a feature coming from the swimmer's geometry. For the model parameters used for the *Chlamydomonas* cell, the alignment angle is determined by $\theta = \arcsin((a_1 - a2)/l) = 30°$. The swimmer therefore should be able to scatter of the wall with any angle $0° < \theta \leq 30°$.

(a) (b)

Figure 4: Antipolar swimmers escape the wall at an angle $\theta > 0$ after aligning (a), while polar ones continuously bump into it with $\theta < 0$ (b).

In addition to the swimmer's polarity, another topic of interest is the effect of wall curvature on the swimmer's "wall-hugging" behavior. Again [13] analyzes the behavior of swimmers with different alignment angles θ concluding that a change in wall curvature has similar effects as changing the swimmer's geometry and thereby θ. Convex walls effectively increase the swimmer's escape angle θ and concave walls decrease it.

2.2.3 Steric wall interactions

The wall interactions are described using a fast rising repulsive potential to approximate a hard wall. For computational speed the Weeks-Chandler-Anderson (WCA) potential is used. It is constructed by shifting up the Lennard-Jones potential and cutting it off at the minimum:

$$\frac{U_\alpha(\delta)}{k_\mathrm{B}T} = \begin{cases} 4\epsilon\left[\left(\frac{a_\alpha}{\delta}\right)^{12} - \left(\frac{a_\alpha}{\delta}\right)^{6}\right] + \epsilon & \text{, if } \delta < 2^{1/6} a_\alpha \\ 0 & \text{, otherwise.} \end{cases} \tag{7}$$

This potential can be seen in figure 3(b). Here δ denotes the distance of the sphere $\alpha \in \{1, 2\}$ to the wall. The parameter ϵ is chosen as $\epsilon = 10$ to get a steep potential wall. The force on the cell is then given by

$$\boldsymbol{F}_{\mathrm{w}} = \boldsymbol{F}_1 + \boldsymbol{F}_2, \text{ with } \boldsymbol{F}_\alpha = -\nabla U_\alpha(\delta), \tag{8}$$

and the torque acting on it

$$\begin{aligned} \boldsymbol{T}_{\mathrm{w}} &= \boldsymbol{T}_1 + \boldsymbol{T}_2 \\ \text{with } \boldsymbol{T}_1 &= (\boldsymbol{r}_1 - \boldsymbol{r}) \times \boldsymbol{F}_1 = \frac{l}{2}(\boldsymbol{e} \times \boldsymbol{F}_1) \\ \text{and } \boldsymbol{T}_2 &= (\boldsymbol{r}_2 - \boldsymbol{r}) \times \boldsymbol{F}_2 = -\frac{l}{2}(\boldsymbol{e} \times \boldsymbol{F}_2). \end{aligned} \tag{9}$$

In the overdamped limit force and torque can be added to the Langevin equations (5) and (6) giving

$$\begin{aligned} \frac{\mathrm{d}\boldsymbol{r}}{\mathrm{d}t} &= v_0 \boldsymbol{e}(t) + \gamma_{\mathrm{w}} \boldsymbol{F}_{\mathrm{w}} + \boldsymbol{\eta}, \\ \frac{\mathrm{d}\boldsymbol{e}}{\mathrm{d}t} &= \left(\frac{\boldsymbol{T}_{\mathrm{w}}}{\tau_{\mathrm{w}}} + \boldsymbol{\xi} \right) \times \boldsymbol{e}. \end{aligned} \tag{10}$$

Here the fluctuation-dissipation theorem (FDT) connects the coefficient of the force and the Gaussian white-noise correlation function $\langle \boldsymbol{\eta}(t) \boldsymbol{\eta}(t') \rangle = 2 k_{\mathrm{B}} T \gamma_{\mathrm{w}} \mathbf{1} \delta(t - t')$. For $\langle \boldsymbol{\xi}(t) \boldsymbol{\xi}(t') \rangle = \frac{2 k_{\mathrm{B}} T}{\tau_{\mathrm{p}}} \mathbf{1} \delta(t - t')$ however, we choose not to use the the FDT to connect persistence time $\tau_{\mathrm{p}} = 5.1\,\mathrm{s}$ [21] and the shear time at the wall $\tau_{\mathrm{w}} = 0.15\,\mathrm{s}$ [22], since the persistence time is connected to the cells active motion and synchronicity of the beating flagella, while the shear time is associated with cell-wall interactions. Hence there is no physical reason to employ the FDT. The value of $v_0 = 60 \mu\mathrm{m\,s^{-1}}$ is based on experimental measurements [11]. Determining a diffusivity for a single *Chlamydomonas* cell is a challenging task. To date only estimates for populations of cells are available, but these values include effects of hydrodynamics and collective motion. So we are forced to give a rough estimate for the diffusivity of an isolated cell. The cell's diffusivity $D = k_{\mathrm{B}} T \gamma_{\mathrm{w}}$ can be estimated as $D \approx \langle x^2 \rangle / (2 \langle \tau \rangle) = L^2 v_0 / (2L) = L v_o / 2$ where L is a typical length scale and v_0 a typical speed. Estimating L to be in the order of a few μm for such swimmers yields diffusivity values in the range of $D = k_{\mathrm{B}} T \gamma_{\mathrm{w}} \sim (10^1 - 10^2) \mu\mathrm{m^2\,s^{-1}}$. Simulations for different values within this range have been performed showing no visible effect of this parameter. Since the cell within confinement is mostly moving ballistic anyways this was to be expected. For historical reasons we chose $k_{\mathrm{B}} T \gamma_{\mathrm{w}} = 20 \mu\mathrm{m^2\,s^{-1}}$ for the simulations to perform analysis on.

2.3 Numerical methods

2.3.1 Time discretization of the stochastic process

To integrate the differential equations (10) a discretization in time is necessary. Here, the Euler method has a sufficient speed and accuracy [20]. The transformation of the differential equations to finite difference equations for times $t_n = t_0 + n\Delta t$

$$\frac{\mathrm{d}\boldsymbol{r}}{\mathrm{d}t} \longrightarrow \frac{\boldsymbol{r}_{n+1} - \boldsymbol{r}_n}{\Delta t}, \qquad \frac{\mathrm{d}\boldsymbol{e}}{\mathrm{d}t} \longrightarrow \frac{\boldsymbol{e}_{n+1} - \boldsymbol{e}_n}{\Delta t} \tag{11}$$

yields a time step

$$\boldsymbol{r}_{n+1} = \boldsymbol{r}_{\boldsymbol{n}} + \Delta t \left(v_0 \boldsymbol{e} + \gamma_\mathrm{w} \boldsymbol{F}\right) + \sqrt{2\Delta t \gamma_\mathrm{w}} \tilde{\boldsymbol{\eta}}, \tag{12}$$

where $\tilde{\boldsymbol{\eta}}$ is again random and its components are drawn from a Gaussian distribution with zero mean and unit standard deviation [4, 23].

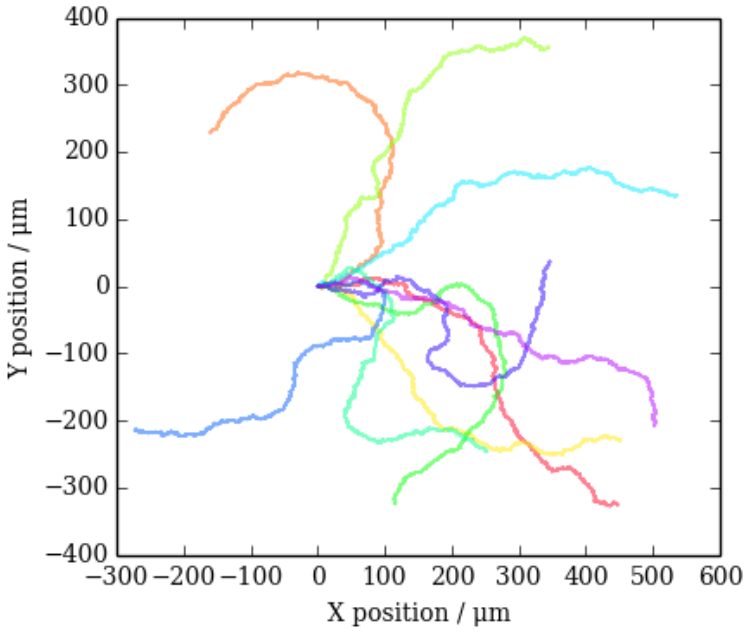

Figure 5: Examples of simulation trajectories without boundaries. A time span of 10s was simulated with all trajectories starting at the origin and the swimmer being oriented to face the positive x-direction.

The cell's orientation has to be normalized, therefore a Lagrange multiplier λ is introduced. The time evolution of a unit vector turning around $\boldsymbol{\omega}$ is:

$$\frac{\mathrm{d}\boldsymbol{e}}{\mathrm{d}t} = \underbrace{\boldsymbol{\omega} \times \boldsymbol{e}}_{\mathfrak{T}} + \lambda \boldsymbol{e}. \tag{13}$$

A step with the Euler method then becomes

$$\boldsymbol{e}_{n+1} = \boldsymbol{e}_n + \Delta t \left(\boldsymbol{\mathfrak{T}} + \lambda \boldsymbol{e}_n\right). \tag{14}$$

The value of λ can be derived as follows:

$$\begin{aligned} \boldsymbol{e}_{n+1}^2 = \boldsymbol{e}_n^2 &+ 2\Delta t \boldsymbol{e}_n \cdot \left(\boldsymbol{\mathfrak{T}} + \lambda \boldsymbol{e}_n\right) \\ &+ \Delta t^2 \left(\boldsymbol{\mathfrak{T}}^2 + 2\lambda \boldsymbol{e}_n \cdot \boldsymbol{\mathfrak{T}} + \lambda^2 \boldsymbol{e}_n^2\right), \end{aligned} \tag{15}$$

since the orientation is normalized $\boldsymbol{e}^2 = 1$ and $\boldsymbol{e} \cdot \boldsymbol{\mathfrak{T}} = -\boldsymbol{e} \cdot (\boldsymbol{e} \times \boldsymbol{\omega}) = 0$, we obtain:

$$\begin{aligned} & \lambda^2 + \frac{2\lambda}{\Delta t} + \boldsymbol{\mathfrak{T}}^2 = 0 \\ \Rightarrow \quad & \lambda = \frac{1}{\Delta t}\left(-1 \pm \sqrt{1 - \Delta t^2 \boldsymbol{\mathfrak{T}}^2}\right). \end{aligned} \tag{16}$$

In the case that $\boldsymbol{\mathfrak{T}} = 0$, the orientation should not change. Therefore the solution with a plus sign in front of the square root has a physical justification and is chosen.

For the equation of motion (10) we get a discrete time step of

$$\boldsymbol{e}_{n+1} = \boldsymbol{e}_n + \left(\Delta t \frac{\boldsymbol{T}_\mathrm{w}}{\tau_\mathrm{w}} + \sqrt{\frac{2\Delta t}{\tau_\mathrm{p}}} \tilde{\boldsymbol{\xi}}\right) \times \boldsymbol{e}_n + \Delta t \lambda \tag{17}$$

with $\tilde{\boldsymbol{\xi}}$ distributed similarly to $\tilde{\boldsymbol{\eta}}$.

Example trajectories produced by this algorithm in free space are shown in figure 5.

2.3.2 Calculating the steric force

Since the "wall-hugging" behavior of *Chlamydomonas reinhardtii* in a confined environment and the effect of different parameters, including the wall's curvature, are of interest here, we study quasi two-dimensional confinement with circular and elliptical boundary. Two dimensional means that the compartment the cell swims in is so shallow, that the cell has basically no space to swim up and down. Elliptical compartments are also chosen because they show a variety of curvatures along the wall and some experimental data exists to compare to [11]. Since the WCA potential in equation (7) is calculated using the distance from the wall it is crucial to the simulations to find the point on the wall which is closest to position (x, y). For an ellipse there are various methods of doing that, one of which will be shown below.

2.3.2.1 Determining the distance to the wall using a quartic formula

An ellipse whose major axis is parallel to the x-axis and minor axis is parallel to the y axis can be written in parametric form

$$x_\mathrm{e}(\varphi) = a\cos\varphi, \quad y_\mathrm{e}(\varphi) = b\sin\varphi \quad \text{with} \quad \varphi \in [0, 2\pi), \tag{18}$$

where a and b are the lengths of the semi-major and semi-minor axis respectively. To find the closest point on the wall the distance δ between (x, y) and $(x_\mathrm{e}, y_\mathrm{e})$ is minimized. The squared distance and its derivative are given by

$$\delta^2(\varphi) = (x - a\cos\varphi)^2 + (y - b\sin\varphi)^2 \tag{19}$$

$$\text{and} \quad \frac{\mathrm{d}(\delta^2)}{\mathrm{d}\varphi} = 2(x - a\cos\varphi)a\sin\varphi - 2(y - b\sin\varphi)b\cos\varphi. \tag{20}$$

To minimize the distance it is necessary that $\mathrm{d}(\delta^2)/\mathrm{d}\varphi \stackrel{!}{=} 0$, yielding

$$xa\sin\varphi - yb\cos\varphi = (a^2 - b^2)\sin\varphi\cos\varphi. \tag{21}$$

This equation can be transformed into a polynomial equation using a transformation[1] $\xi = \tan(\varphi/2)$ which is bijective for $\varphi \in (-\pi, \pi)$, and therefore it is sufficient to look at the first quadrant ($x \geq 0$ and $y \geq 0$), since the result can simply be mirrored into the other quadrants, due to the ellipse symmetry. This gives values $\varphi \in [0, \pi/2]$ and $\xi \in [0, 1]$, making the transformation well defined and limiting the calculation results to a numerically favorable interval. Making use of the identities (for the derivation see appendix A.1)

$$\cos\varphi = \frac{1 - \xi^2}{1 + \xi^2} \quad \text{and} \quad \sin\varphi = \frac{2\xi}{1 + \xi^2} \tag{22}$$

equation (21) transforms into a quartic formula (fourth degree polynomial) for t:

$$yb\xi^4 + (2xa + 2c)\xi^3 + (2xa - 2c)\xi - yb = 0 \tag{23}$$

with $c = a^2 - b^2$. Since quartic formulas have analytic solutions the four possible solutions for ξ can be computed using standard solving methods. One of the solutions

[1] The use of this transformation was inspired by a piece of work from Robert Estalella from the University of Barcelona accessible under `http://www.am.ub.edu/~robert/Documents/ellipse.pdf` [Accessed 15 September 2016].

then gives the closest point

$$\begin{aligned} x_e &= a\cos\varphi = a\frac{1-\xi^2}{1+\xi^2}, \\ y_e &= b\sin\varphi = b\frac{2\xi}{1+\xi^2}. \end{aligned} \tag{24}$$

The distance to the wall $\delta = \sqrt{(x-x_e)^2 + (y-y_e^2)}$ can then be used with equation (8) to determine the steric force

$$\boldsymbol{F}_\alpha = -\nabla U_\alpha = 24\epsilon \left(\frac{a_\alpha}{\delta}\right)^6 \left[2\left(\frac{a_\alpha}{\delta}\right)^6 - 1\right] \delta^{-1}\boldsymbol{n}, \tag{25}$$

where $\boldsymbol{n}$ is the unit vector pointing inwards perpendicular to the wall at (x_e, y_e).

3 Simulation results

3.1 Circular compartments

Simulations of the model introduced in section 2.2 have been carried out for circular, quasi 2d compartments. They show a "wall-hugging" effect, that is, the probability of finding the swimmer near a concave wall is greatly increased compared to finding it at some other position in the bulk [11]. The relative probability density can be seen in figure 6 and 7. The probability exhibits a rather flat plateau in the "bulk" of the chamber. In close proximity of the boundary, however, the probability $P(r)$ exhibits a steep peak. This peak represents the "wall-hugging" effect.

These results reproduce the experimental measurements quantitatively for different compartment sizes (see figure 6) and therefore different wall curvatures.

Defining the probability to be in a wall-hugging state Φ as the increase in area under the radial probability distribution $P(r)$ close to the wall as compared to the plateau height (see figure 8) gives the possibility to quantify this effect in a single number. The probability to be in a "wall-hugging" state, as seen in figure 9, monotonically increases with curvature $\kappa = R^{-1}$, where R is the compartment radius [11]. From a compartment radius of $\sim 100\mu$m, up to the maximum compartment

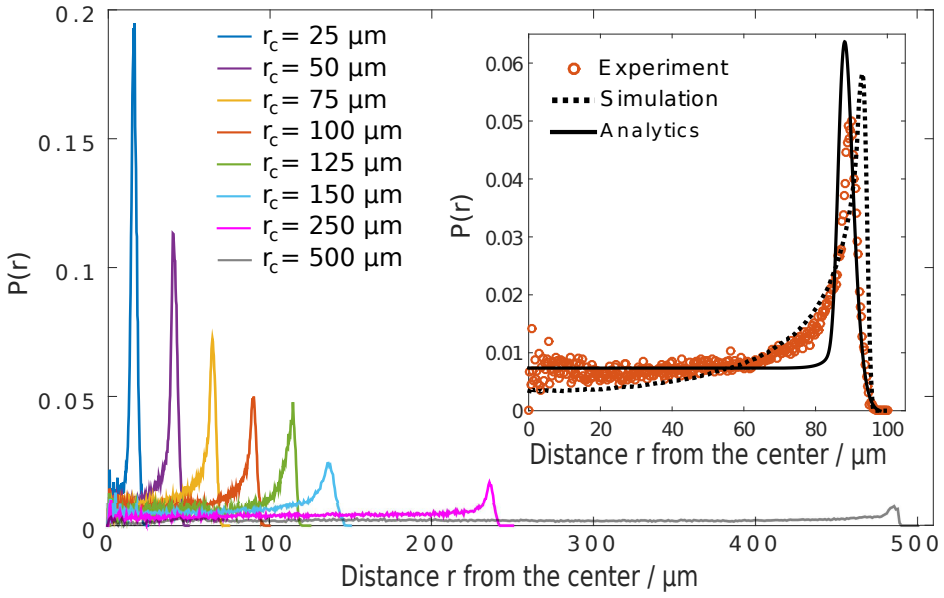

Figure 6: Experimentally measured radial probability $P(r)$ of the cells position for different compartment radii normalized so that $\int P(r)\mathrm{d}r = 1$. The inset shows a comparison of experimental data, simulations and analytics for a compartments of radius $r_c = 100\mu$m. Image adapted from [11].

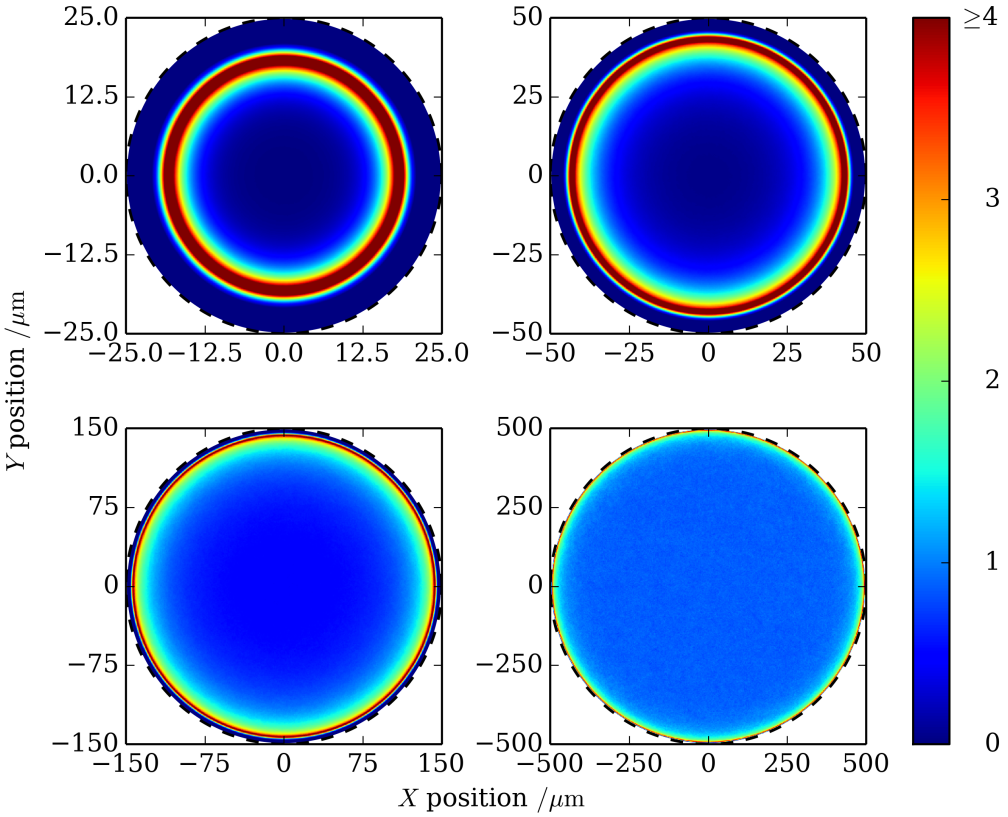

Figure 7: Relative probability density in circular confinements of different size from simulations according to section 2.3 (dotted line denotes the compartment wall). The relative probability density is normalized with $p(\boldsymbol{x}) = n_{\mathrm{bin}} A_{\mathrm{tot}}/(A_{\mathrm{bin}} \Sigma n_{\mathrm{bin}})$, where n_{bin} is the number of counted trajectory points in a square bin, $A_{\mathrm{bin}} = (R/500)^2$ is the area of said bin and $A_{\mathrm{tot}} = \pi R^2$ is the area of the compartment, with radius R.

size used in experiments (500μm), Φ scales linearly with the curvature, falling below this $1/R$ behavior for smaller compartments. Simulations and experimental results using a round pillar in the center of the compartment suggest that the swimmer scatters off convex interfaces almost immediately, while getting trapped at concave walls (see figure A.1).

Because simulations and experiments in circular compartments suggest a strong link between the wall-hugging effect and the wall curvature, more complex geometries like elliptical chambers are of interest, since they show a continuous variation of wall curvatures.

A swimmer consisting of just one sphere is not able to experience a torque at the wall, making it rely just on random fluctuations to escape the border region. Thereby, it is impossible to find a value of τ_{p} that reproduces the strength of "wall-hugging" and the tumble time seen in experiments by just simulating a spherical

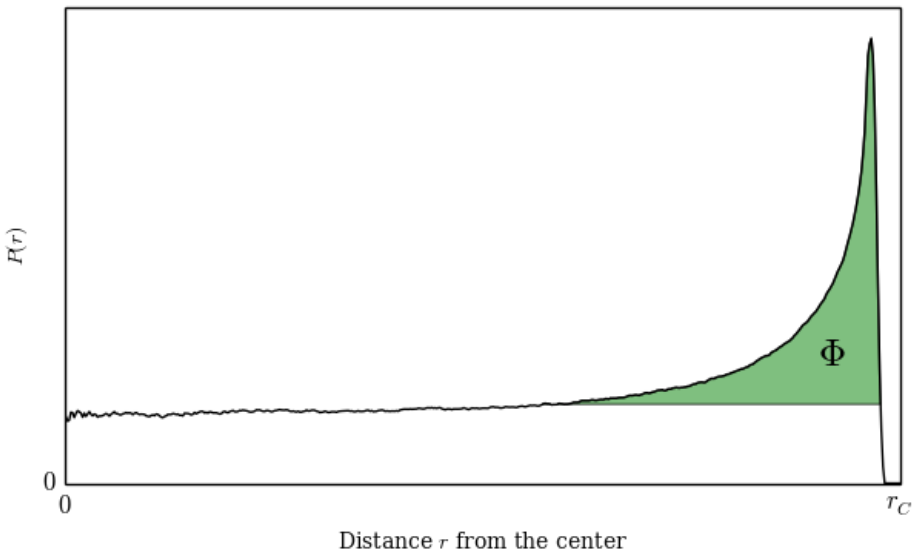

Figure 8: Visualization of the meaning of the wall hugging probability. Φ measures the "area" under the radial probability distribution, that gets added to the plateau near the wall, that is the probability that the swimmer does not swim around freely, but got stuck at the wall for a certain time.

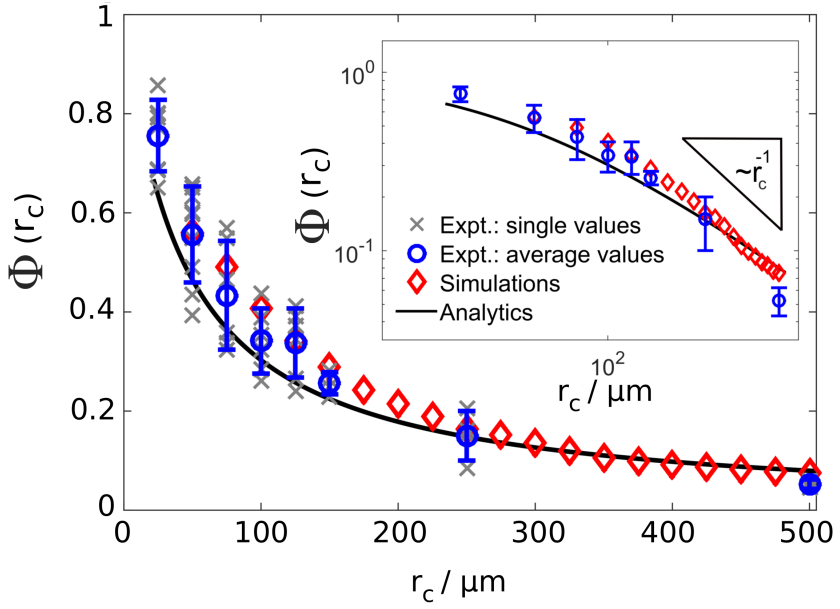

Figure 9: The wall-hugging probability of the cell according to the definition in [11] for different compartment sizes. Image adapted from [11].

swimmer. Simulations of a spherical swimmer using the measured value of τ_{p} have been carried out, showing completely different behavior, from what is observed in experiments. The dumbbell swimmer introduced in section 2.2 mainly escapes the wall due to the torque acting on it when swimming into it, making it show a weaker "wall-hugging" effect.

3.2 Relative probability density in elliptical compartments

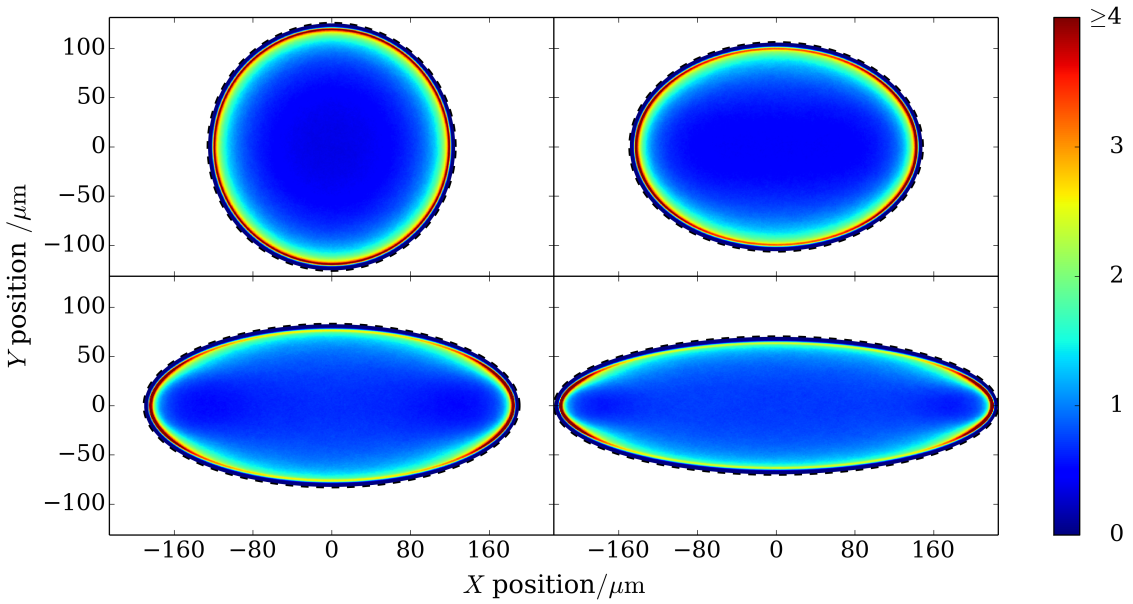

Figure 10: Relative probability density in elliptical confinements of different eccentricity and area $A_{\text{tot}} = 50000(\mu\text{m})^2$ from simulations (dotted line denotes the compartment wall). The relative probability density is normalized similarly to figure 7 with $A_{\text{bin}} = ab/500^2$ and $A_{\text{tot}} = \pi ab$, where a and b are the semi-major and minor axes. Eccentricity values shown are 0.00, 0.70, 0.90 and 0.95 going from left to right, top to bottom.

To verify the curvature dependencies of the observed "wall-hugging" behavior the simulation's code was modified to deal with an elliptical confinement, giving information for a continuous interval of curvatures at once. The strength of this effect rises with the ellipse's eccentricity

$$\varepsilon = \sqrt{1 - \left(\frac{b}{a}\right)^2}, \tag{26}$$

where a and b denote the length of the semi-major and minor axis, respectively, since ellipses show an increasing range of wall curvatures

$$\kappa \in \left[\frac{b}{a^2}, \frac{a}{b^2}\right] \tag{27}$$

for larger eccentricities. The relative probability density obtained through simulations for elliptical compartments of different eccentricity is shown in figure 10. Here, the compartment area is kept constant, and the eccentricity is increased from $\varepsilon = 0$

up to $\varepsilon = 0.95$ showing a shift of probability density from the area near points with a local curvature of $\kappa = b/(a^2)$ towards locations close to the apex with $\kappa = a/(b^2)$. This shift becomes more and more prominent as the range of curvature increases with eccentricity. Simulation results for elliptical compartments confirm the observation from the circular ones that the swimmer is more likely to be found at a wall of higher curvature. For elliptical compartments this means that the cell is most likely to be found near the antipodal points of the major axis.

3.2.1 Comparison with experimental results

Comparison of simulations and experimental results for circular compartments have been done in [11] and can be seen in figure 6. For elliptical compartments, experimentally measured trajectory points were kindly supplied from the experiments of [11] making it possible to compare them with simulation results. Relative probability density heat maps can bee seen in figure 11 for experiments and simulation results in elliptical compartments with the same geometry and size. Experiments and simulations show similar behavior, with increased probability to find the cell near the compartment wall. This effect is greatly increased near the apex regions, growing weaker upon decreasing curvature. It is hard to quantify the level of agreement just by comparing the heat maps, therefore, it will be analyzed in more detail in the following.

3.3 Maximum probability density along rays

To quantify the effect of the walls curvature on the probability density the relative probability density is evaluated along rays emerging from the center of the ellipse going outward at constant angle θ. This method is visualized in figure 12. Looking at the peak heights of the probability along different rays gives an estimate of how strong the "wall-hugging" effect is depending on the walls curvature, since the maximum always occurs in close proximity to the wall. Even though the peak height is not to be compared to the "wall-hugging" probability in figure 9 without caution, because they measure different things, it makes quantifying the agreement of simulations and experiments relatively easy. It yields some intuition of how the wall curvature influences the swimmers behavior. However, this is not as useful of a measure as the "wall-hugging" effect defined in section 3.1 for circular compartments, but a local variant of the "wall-hugging" probability will be defined later in section 3.5. Figure 13 shows the maximum probability along the ray passing the wall at a point of curvature κ for different areas and eccentricities of the confining ellipse. For

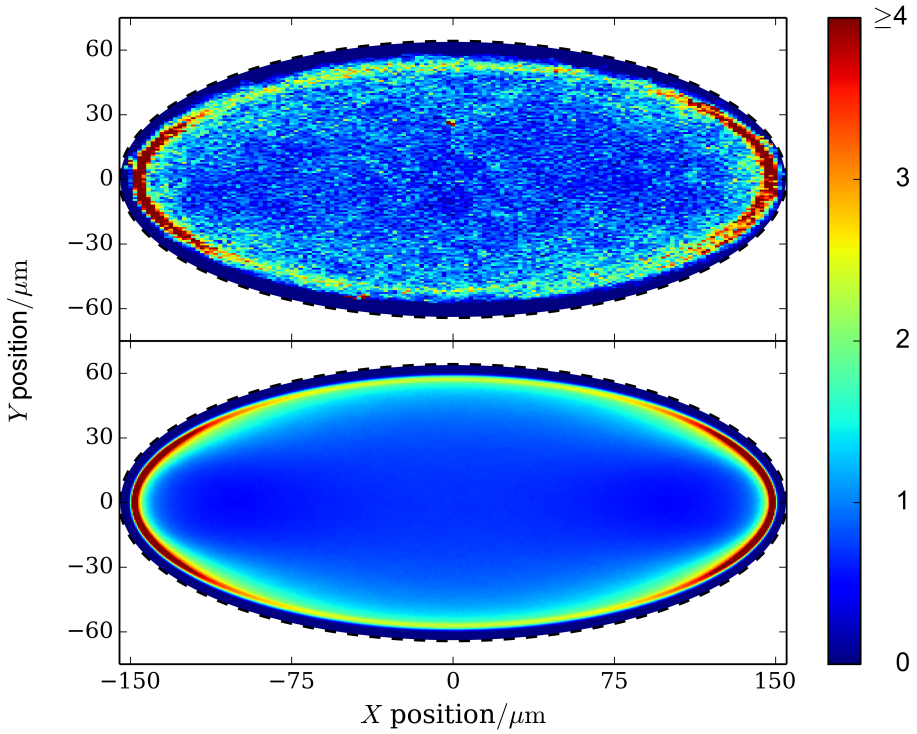

Figure 11: Relative probability density in an elliptical confinement of eccentricity $\varepsilon = 0.91$ and an area of $A_{\text{tot}} = 31316.7(\mu\text{m})^2$. Probability density derived from experimentally measured and simulated trajectories is shown on the top and bottom panel, respectively. The probability density is normalized to the area as in figure 10 with the resolution of bins for experimental values decreased to 150 bins vertically and horizontally because of less available statistics from the experiment.

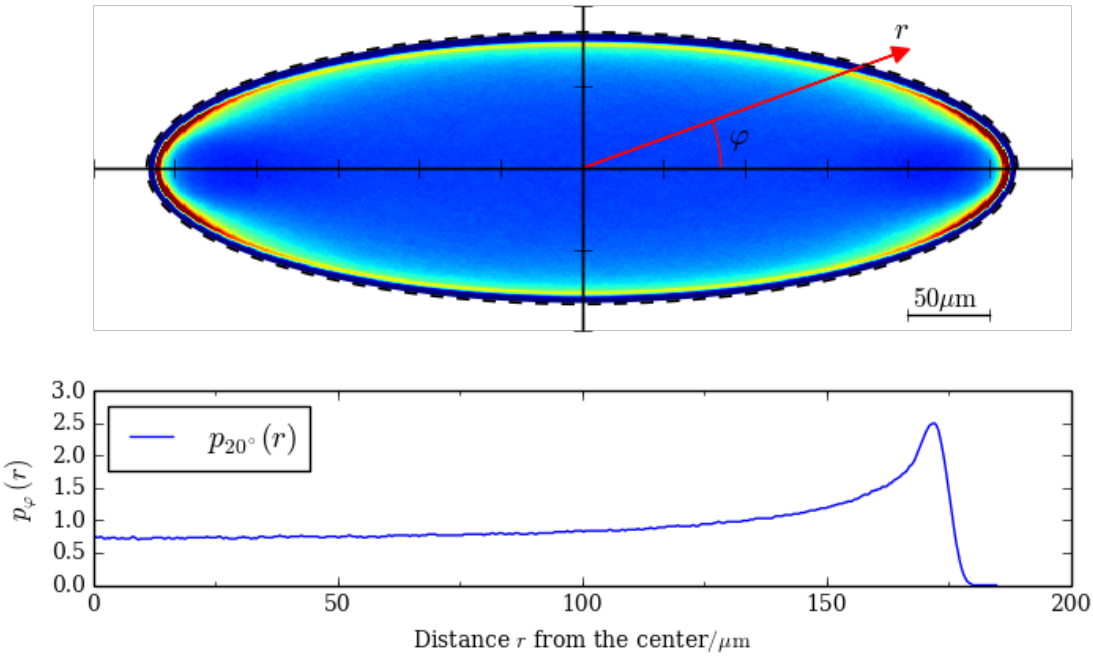

Figure 12: Evaluating the relative probability density in the compartment along a ray going out from the center of the ellipse (top panel) produces curves like the one shown in the bottom. Although they look similar to the radial probability distribution in a circular compartment, comparing them is not appropriate since the rays are not perpendicular to the compartment wall. This method however has proven quite useful to quantify the agreement of simulation results with experimental data by comparing the peak heights of these curves for different angles and repeating the procedure for all quadrants gives an approximation of the statistical uncertainty.

curvatures in a range $0.002\mu\text{m}^{-1} \lesssim \kappa \lesssim 0.015\mu\text{m}^{-1}$ the calculated values seem to grow approximately linear with κ with their slope decreasing for higher curvatures. This is similar to what was found for Φ in section 3.1 and shown in figure 9 where the biggest circular compartment had a radius of $r_\text{c} = 500\mu\text{m}$ giving a curvature of the before mentioned $\kappa = r_\text{c}^{-1} = 0.002\mu\text{m}^{-1}$. Below this curvature the "wall-hugging" effect seems to stay at a constant strength. Note that, of course, for bigger compartments the ratio of the ellipses circumference to available area decreases, so naturally the cell is less likely to be found at the wall, therefore the probability density is normalized to the area such that

$$\int p(\boldsymbol{r})\mathrm{d}\boldsymbol{r} = A_\text{tot} \tag{28}$$

as explained in figure 7 and 10, making the curves in figure 13 collapse almost completely.

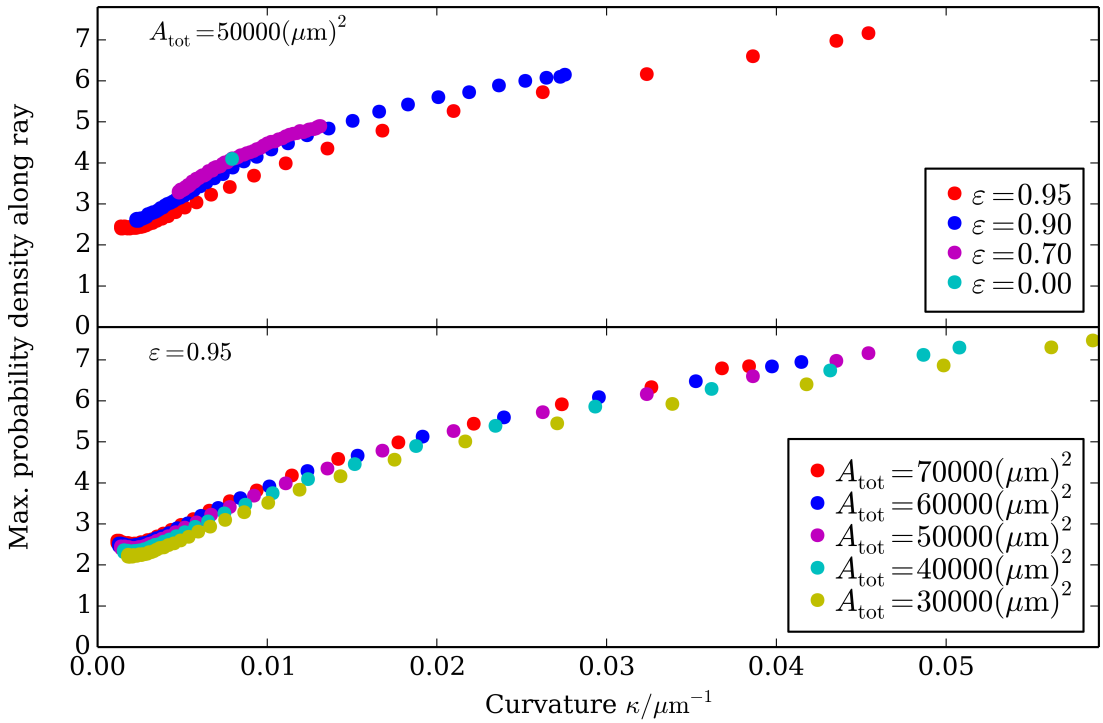

Figure 13: The relative probability density peak height along different rays in different elliptical compartments evaluated as explained in figure 12. The value of curvature κ corresponds to the local curvature of the ellipse, where the ray passes the compartment wall, resulting in a range of values for elliptical and only one value of κ for the circular compartment.

3.3.1 Comparison with experimental results: Maximum probability density along rays

The comparison for experimental measurements and simulations of the maximum probability density along the rays with origin at the ellipses center and passing the ellipse at the wall point with local curvature κ is shown in figure 14. The simulations seem to predict the slope of the curve with an accuracy within the uncertainty of the experiment, in the entire range of curvatures. The simulations also capture the crossover from a linear slope for $\kappa \leq 0.01(\mu\mathrm{m})^{-1}$ to a second linear regime with a smaller slope. The simulations however seem to overestimate the peak height, which was already observable for the radial probability distribution in circular compartments, as it can be seen in the inset of figure 6. This results in a vertical shift of the simulation results with respect to the experiments.

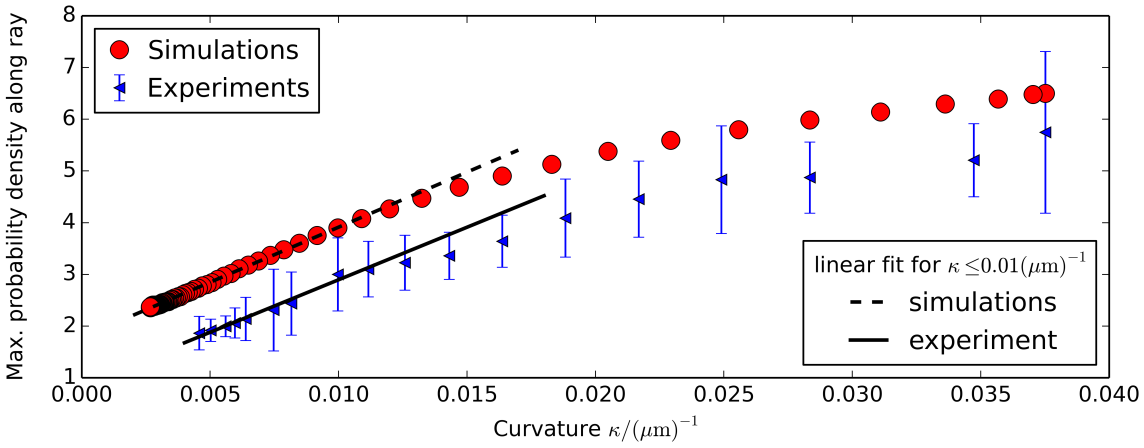

Figure 14: The relative probability density peak height evaluated as explained in section 3.3 for experimental measurements compared to simulation results and a linear fit for values of $\kappa \leq 0.01(\mu\mathrm{m})^{-1}$. Simulations and experiments were carried out in an elliptical compartment of eccentricity $\varepsilon = 0.91$ and an area of $A_{\mathrm{tot}} = 31316.7(\mu\mathrm{m})^2$. The error bars denote the uncertainty of values when the peak height is evaluated in all four quadrants separately.

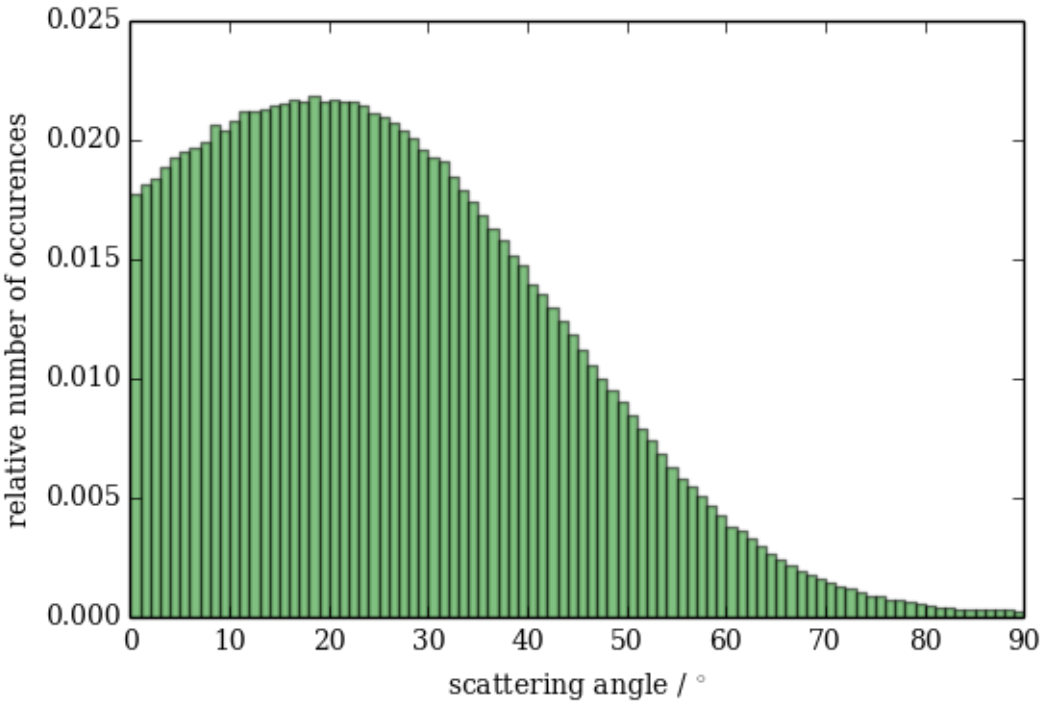

Figure 15: The distribution of swimming angles after scattering off a flat wall. Values were taken at a distance of $(20 \pm 2.5)\mu$m away from the wall, after the swimmer scattered off to ensure the swimmer is no longer in contact with the wall and has finished the turning process.

3.4 Scattering Angle

Since Wysocki *et al.* [13] claim that there is an equivalence of shape asymmetry and wall curvature, that is, a concave wall effectively decreases the swimmer's escape or scattering angle, the scattering angle of the simulated model is measured similarly to what has been done experimentally in [22]. The swimmer is confined within a straight channel, with solid walls in the y-direction and periodic boundary condition in the x-direction. After each scattering event recorded off the wall the angle spanned by the x-axis and the swimming direction is recorded. This is done for a channel of width 300μm. The scattering angle is recorded when the cell is separated by a distance of $(20 \pm 2.5)\mu$m from the wall. This distance is chosen to directly compare with experimental values from [22], where they considered a distance of 20μm from the wall, and also to make sure the swimmer has finished turning at the wall and is swimming freely. This is surely the case since at this distance the swimmer is not subject to the wall potential any more because the model only considers steric interactions. These measurements yield an angle distribution that is shown in figure 15, with a mode for the scattering angle of $\sim 18°$ which is close to what was experimentally found in [22, 24].

3.5 Wall hugging is affected by local curvature and available space

To compare the wall hugging effect in elliptical and circular compartments the probability distribution along a ray of constant angle θ like in section 3.3 is no viable tool since these rays do not intersect the compartment border normally for ellipses. The appropriate comparison would be a the distribution perpendicular to the wall. This is done by finding the osculating circles for different points of curvature κ along the elliptical compartment's wall and comparing the distribution perpendicular to the wall with the distribution of a circular compartment with the same size as the osculating circle. This procedure is explained in detail in figure 16. Since one ellipse shows a range of curvatures $\kappa \in [a/(b^2), b/(a^2)]$ it yields data to compare with multiple, differently sized circular compartments as shown in figure 17. By comparing the resulting probability distribution curves from one ellipse with different circular compartments as done in figure 17(c) one gets to the impression that there always is one point of curvature where the probability distribution of the ellipse and the corresponding circular compartment match best. It turns out that this is always the case at the point of curvature where the osculating circle has the same area as the ellipse.

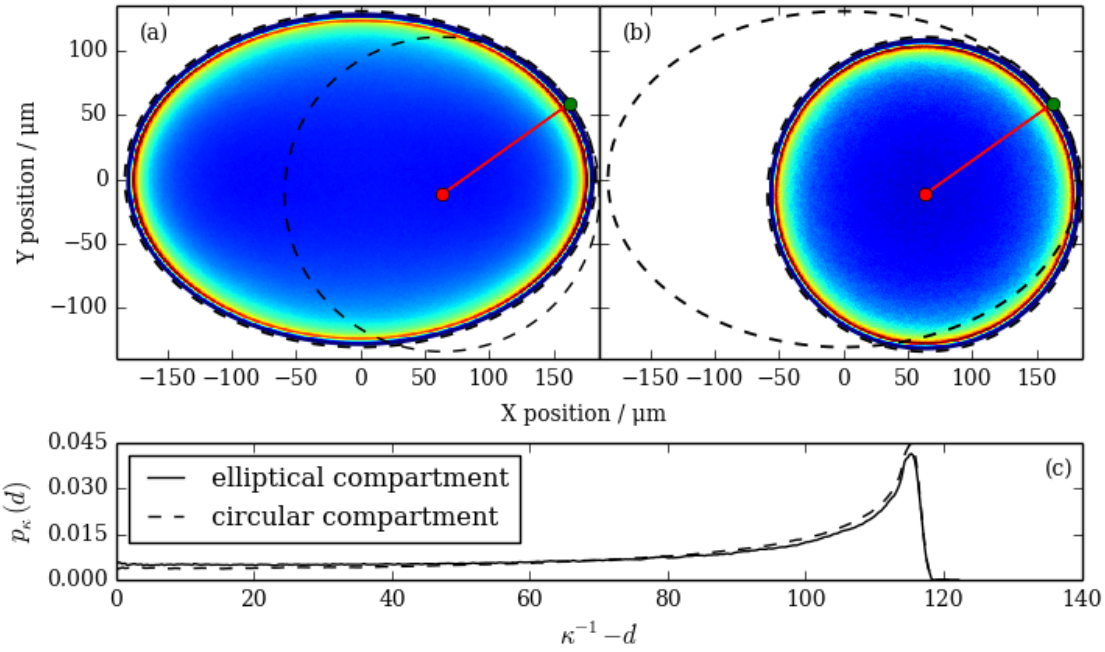

Figure 16: The relative probability density inside an ellipse is shown in panel (a). To be able to compare with circular compartments in a meaningful way, we consider the osculating circle tangent to the ellipse at the point of curvature κ. This osculating circle is shown using a dashed line in (a) with the tangent point marked in green and the center of the osculating circle in red. The probability distribution is evaluated along the line of length κ^{-1} connecting these two points at distance d to the wall. Panel (b) shows the relative probability density in a circular compartment with the radius of the osculating circle from (a). The outline of the elliptical compartment is shown with a dashed line as a reference. The probability distribution is then evaluated similarly to what is done in (a). Panel (c) shows the comparison of the resulting probability distributions normalized equally. This method however has its limitations. When the center of the osculating circle (the circle of radius κ^{-1} being tangent to the ellipse at the point of curvature κ), which is the red dot in panel (a), comes too close to the elliptic wall on the other side, the probability distribution is influenced by the opposing wall. A demonstration of this problem is shown in figure 17.

To quantify this agreement, the quantity

$$\int_0^{r_c} \sqrt{(P_{\text{ellipse}} - P_{\text{circle}})^2}\,\mathrm{d}r \tag{29}$$

is calculated for different points of curvature, and thereby differently sized osculating circles and corresponding circular compartments. The value of this difference always reaches its minimum at the point of curvature where $A_{\text{circle}} \approx A_{\text{ellipse}}$. To show this universal behavior in figure 18 the curvature κ, and thereby the radius of the osculating circles, are given in units of this characteristic radius R_{eq} of a circle

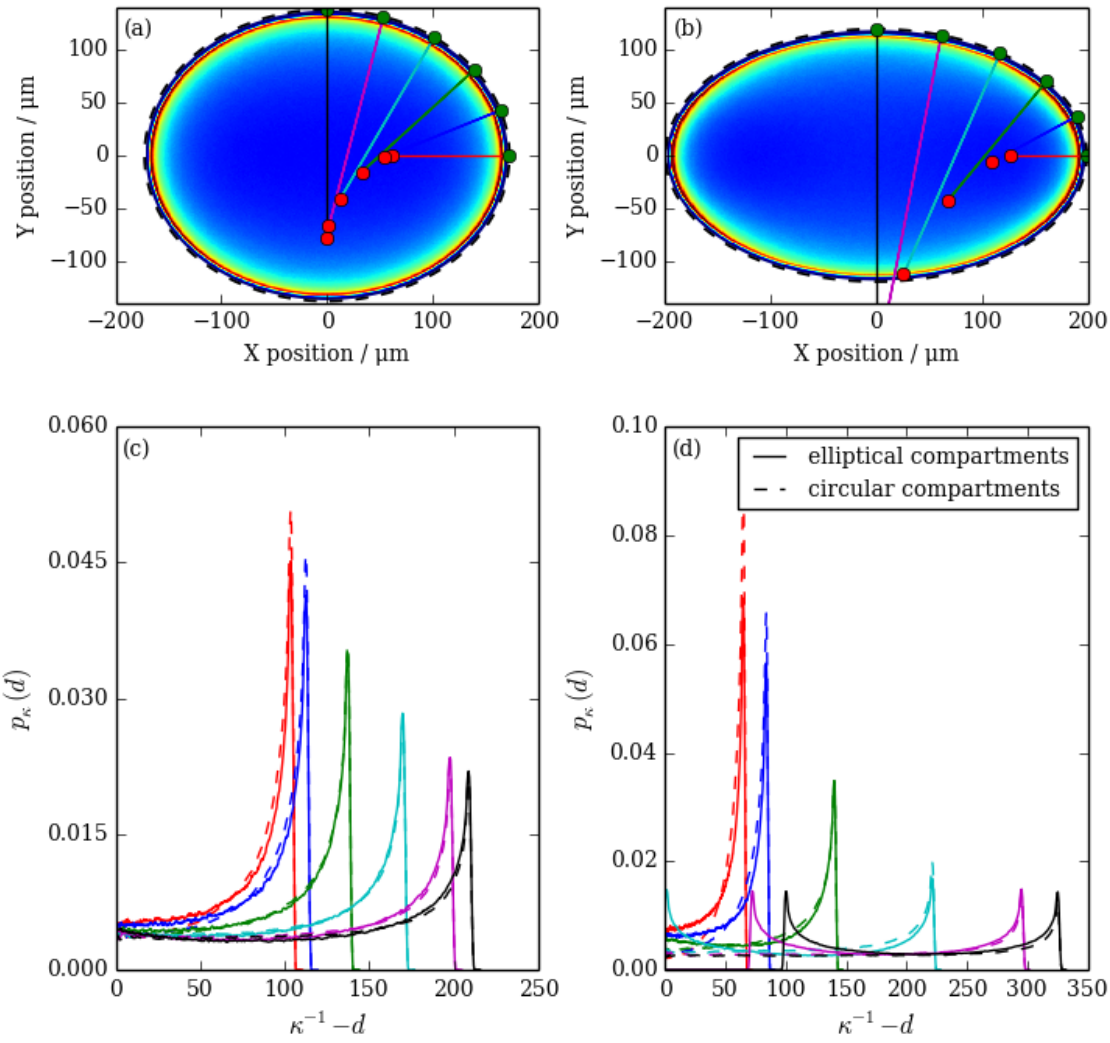

Figure 17: Panel (a) and (c) show the use of the method shown in figure 16 multiple times along the ellipse starting at the apex and going down in curvature. The distance along which the probability distribution needs to be evaluated grows, as one can see in (a). This yields a range of curves for one ellipse, all comparable to their corresponding circular compartments as done in (c). Panel (b) shows when this method starts to break down. When $d = \kappa^{-1}$ becomes so large that the center of the corresponding osculating circles (marked in red) gets so close to the compartment border the probability distribution along the connecting line is influenced by the opposing wall, or even cut off. The resulting partially cut off probability distributions can be seen in panel (d). For high-eccentricity ellipses, this problem limits the range of curvatures where a meaningful comparison with circles can be done.

covering the same area as the examined ellipse.

$$A_{\text{ellipse}} = A_{\text{circle}} = \pi R_{\text{eq}}^2 \implies R_{\text{eq}} = \sqrt{A_{\text{ellipse}}/\pi}. \tag{30}$$

The results of this procedure for multiple compartments of different eccentricities

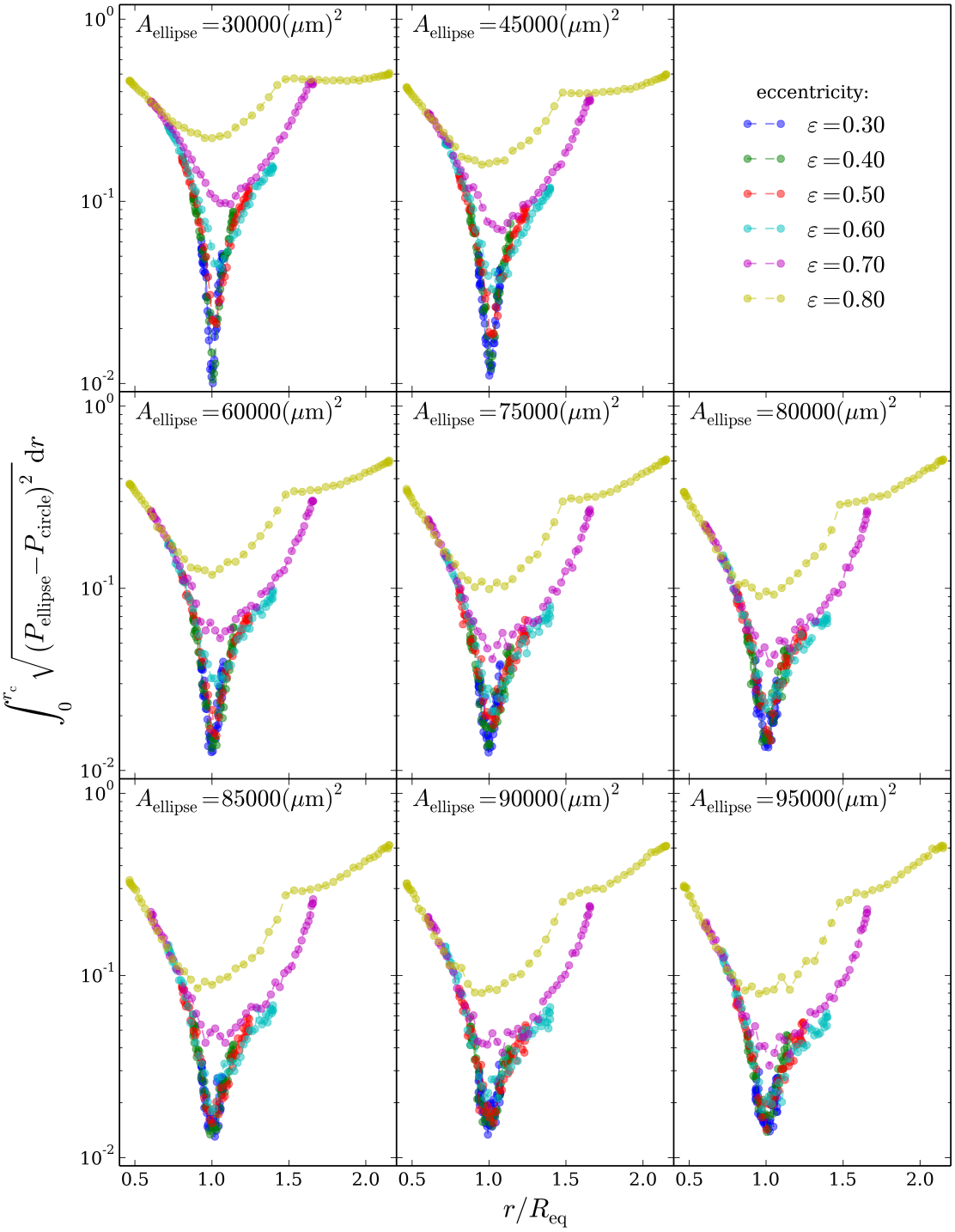

Figure 18: The level of agreement $\int_0^{r_c} \sqrt{(P_{\text{ellipse}} - P_{\text{circle}})^2} dr$ of relative probability distributions perpendicular to the wall for different radii of curvature $r = \kappa^{-1}$ along elliptical compartment walls with the radial probability distribution in circular compartments when both are normalized to $\int_0^{r_c} P_{\text{ellipse/circle}} dr = 1$. The radius of curvature is normalized to the radius where the circle covers the same area as the elliptical compartment.

and areas are shown in figure 18. All data sets seem to show a minimum, in close proximity of $r/R_{\text{eq}} = 1$. This means that probability distributions for a fixed curvature in circular compartments and elliptical ones are in fact most similarly shaped when ellipse and circle cover the same amount of area, seemingly independently of how big this area actually is and how eccentric the ellipse is. The flattening of the curve for large eccentricities and small areas can be explained with the limits of this method for obtaining P_{ellipse}, as shown in figure 17.

3.6 Broken detailed balance in elliptical compartments

Although probability-density heat maps like in figure 7, 10 and 11 nicely show where the swimmer is likely to be found and where it spends most of the time, they give no indication where the swimmer is most likely to move in the future. To visualize the flow of probability the compartment is, similarly to the creation of the heat maps, divided into bins, but now instead of measuring how much time the swimmer spends in a bin over the course of one run, its swimming direction at this point is averaged over time $\langle \boldsymbol{e}(\boldsymbol{x}) \rangle_t$. A visualization of this vector field for compartments of different eccentricity is shown in figure 19.

In circular compartments $\langle \boldsymbol{e}(\boldsymbol{x}) \rangle_t \approx 0$ is homogeneously observed in the compartment, meaning that there is no net flow of probability and no preferred orientation once a stationary distribution is reached. This indicates that detailed balance holds, that is, the transition from one state to another is equally likely as going exactly the other way round. For circular compartments there can practically not be a preferred angular direction because of their radial symmetry, so a probability flux in angular direction makes no sense. The only spacial direction left for a flux in probability would be radial. Since probability needs to be conserved the only possibility for that, given there are no sources and sinks within the confinement is a vortex. Since vortices need at least two spacial directions to exist they cannot exist only in radial direction, resulting in the fact that circular compartments do not allow any probability flux.

With increasing eccentricity much more interesting results can be observed. Unlike in the circular compartment case, distinct preferred orientations emerge in certain parts of the compartment, forming a vortex in every quadrant. This is also observable in the normalized orientation field's rotation $\nabla \times (\langle \boldsymbol{e}(\boldsymbol{x}) \rangle_t / |\langle \boldsymbol{e}(\boldsymbol{x}) \rangle_t|)$ also shown in figure 19 for a circular and elliptical compartments for comparison. Fluxes of probability are the hallmark of nonequilibrium and indicate without any ambiguity that detailed balance is broken. The swimmer is more likely to be oriented in certain directions at certain positions. The ensuing vortices fill the whole

ellipse for lower eccentricity but are rather separated for eccentricities $\varepsilon \gtrsim 0.8$, leaving an area in the middle where $\langle \boldsymbol{e}(\boldsymbol{x}) \rangle_t \approx 0$ again. The simplest explanation for all the observed effects is that the swimmer, when approaching the compartment wall at high local curvature, tends to swim down the curvature gradient along the wall, until low curvature makes an escape from the wall more likely. The observed vortices then have to arise because of conservation of probability. This may also explain the stagnation in the drop of peak height for low curvature in figure 13, since the cell tends to swim towards these areas.

The breaking of detailed balance is most likely also the cause for the small difference in peak heights when considering compartments of different eccentricity like in the upper part of figure 13 since the breaking of detailed balance causes a change in the global dynamics, giving the swimmer a preferred direction in some parts of the compartment, while the peak height is measured only locally. "Wall hugging" effects, therefore, cannot only be linked to local curvature, even though it does seem to be the dominant factor, but they are also influenced by global dynamics. How far the system is away from detailed balance seems to be determined by the local curvature gradient. Ellipses of large eccentricity have much higher gradients of curvature near the antipodal points of the major axis than near the ones of the minor axis. This could be an explanation why the curves in the bottom of figure 13 collapse much better than those in the top, since changing the ellipses area does not change the range of curvature nearly as much as changing the eccentricity does, allowing much higher curvature gradients. This is also supported by the fact that in both the upper and lower plot of figure 13 the elliptical compartment with the biggest range of curvature always shows the lowest probability density at the wall.

The plots in figure 19 always show an average swimming direction pointing perpendicularly away from the wall when in contact with it. This is an artifact of the fact that the swimmers position is measured between the centers of the two spheres (see section 2.2). This results in the swimmer being detected at $a_1 + l/2$ distance from the wall, when swimming "head-first" into it, but only $a_2 + l/2$ distance when facing away from it (with the swimmer being modeled as antipolar meaning $a_1 > a_2$). The latter state is incredibly rare, since the probability density so close to the wall is nearly zero (see figure 6) Thus, these points, showing a strong bias in orientation are made up of only a statistically not significant number of points when the swimmer was brought into such an unlikely state by fluctuations. But since the only orientation it can have so "close" to the wall is facing away from it the orientation seems biased.

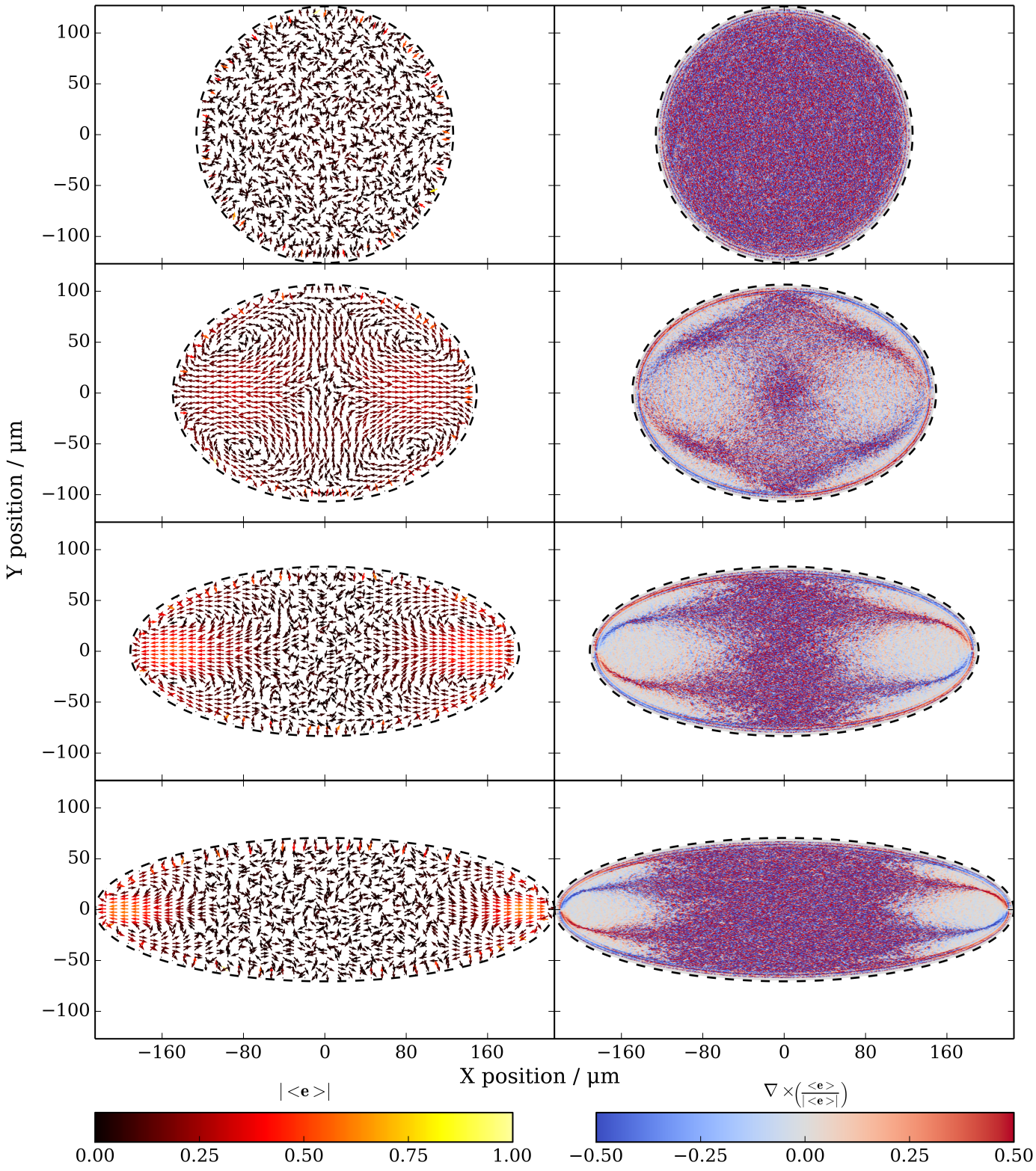

Figure 19: Broken detailed balance in elliptical compartments. Compartment eccentricities and areas are the same as in figure 10. The left side shows the time averaged swimming direction in the compartment $\langle \boldsymbol{e}(\boldsymbol{x}) \rangle_t$ with the norm of the vector represented as its color. The right side shows the rotation corresponding to these vector fields, which is a pseudo-scalar for two dimensional fields. Positive values correspond to counterclockwise rotations.

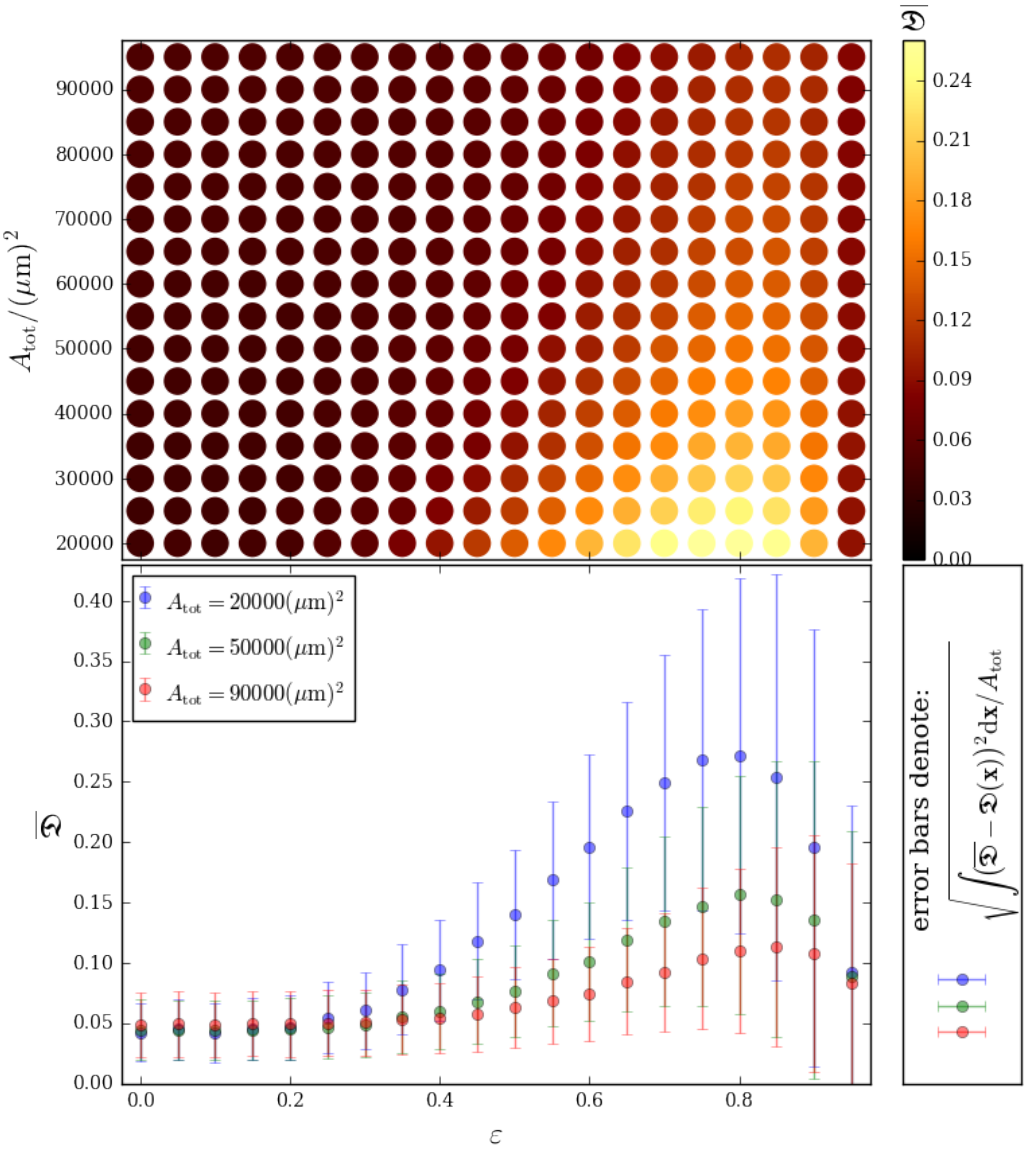

Figure 20: The measure $\overline{\mathfrak{D}} = \int \mathfrak{D}(\boldsymbol{x})\mathrm{d}\boldsymbol{x}/A_{\text{tot}}$, with $\mathfrak{D}(\boldsymbol{x}) = |\langle \boldsymbol{e}(\boldsymbol{x})\rangle_t|$ for simulations of elliptical compartments of different size and eccentricity. With higher $\overline{\mathfrak{D}}$ the more likely it is to predict the cells swimming direction from its position according to what is shown in figure 19. The error bars in the bottom image additionally shows how much this measure varies over the whole area of the compartment using the error bars. The compartments all show a peak in $\mathfrak{D}$, with increasing ε after which $\mathfrak{D}$ goes down rapidly, but with the variations in $\mathfrak{D}$ rising over the whole range of ε.

To quantify the emergence of probability fluxes we consider the norm of the time averaged orintation vector

$$\mathfrak{D}(\boldsymbol{x}) = |\left\langle \boldsymbol{e}(\boldsymbol{x})\right\rangle_t|. \tag{31}$$

The normalized integral of this field over the compartment area

$$\overline{\mathfrak{D}} = \int \mathfrak{D}(\boldsymbol{x})\mathrm{d}\boldsymbol{x}/A_{\mathrm{tot}} \tag{32}$$

then can be seen as a measure of how strong the probability fluxes in the whole system are. The results of this integration are shown in figure 20 for different eccentricities and areas. To avoid the above described artifacts at the border this measure is calculated only where the swimmer is not touching the wall, so when it is more than one swimmer length $(a_1 + l + a_2)$ away from the wall. A standard deviation

$$\sqrt{\int \left(\overline{\mathfrak{D}} - \mathfrak{D}(\mathbf{x})\right)^2 \mathrm{d}\mathbf{x}/A_{\mathrm{tot}}} \tag{33}$$

is shown there as error bars. This is of course no real standard deviation, but its growth can be seen as a measure of the separation of the vortices with increasing eccentricity separating areas far from detailed balance from those closer to it. So the overall concentration of probability flux for the swimmer's orientation rises up to a certain eccentricity, where curvature gradients along the wall are relatively high along the whole compartment wall and the resulting vortices all fill a whole quarter of the ellipse. The value of $\overline{\mathfrak{D}}$ goes down again when the difference in curvature gradient along the ellipse wall increases, separating areas with no preferred orientation from those with a stronger bias. This explains the rise of the variance of $\overline{\mathfrak{D}}$ depicted using the error bars in the bottom of figure 20. Since the breaking of detailed balance in this case is an effect induced by the confinement (no preferred orientation is to be expected in free space) the overall strength of the effect goes down with less confining geometries, meaning bigger compartments.

4 Conclusions

We have studied a minimal model of *Chlamydomonas reinhardtii* that can reproduce the experimentally observed curvature-guided motion of *Chlamydomonas reinhardtii* in strong confinement. The "wall-hugging" probability, defined as Φ, for circular compartments is reproduced within the margin of error as it can be seen in figure 6 and the slope of peak heights for elliptical compartments is almost identical as shown in figure 14, even though they exhibit a slight offset when considering the absolute values. The dominant scattering angle of $\sim 18°$ at flat walls (see section 3.4) is consistent with what was measured in [22] ($12° - 20°$ for mutants with different flagella length) and in [24]($12° - 20°$ for different mutants), while [24] aims to reproduce these with a more complex model using three spheres connected by springs and including hydrodynamics. A simpler model of swimmer consisting only of a single sphere would not be able to experience a torque from the wall leading to different dynamics with the swimmer continuously bumping into the wall, because it cannot escape for very long times, when the persistence time τ_p is kept at realistic values. This not only results in enormous probabilities to find the swimmer at a wall, but also to a qualitatively different curvature dependence of the probability peak height (as it can be seen in figure A.2) compared to a real swimmer. The simulations with a single-sphere swimmer were carried out by simply removing the smaller sphere of the swimmer by setting a_2 and l to zero, which results in automatically disabling the wall-induced torque acting on the swimmer. The strength of the effect is probably adjustable to levels similar to what was measured in the experiment by heavily adjusting the model parameters. Doing so, however, is not really appropriate since the biggest strength of the two sphere model is that it reproduces the increased probability density of the experiment reasonably well using only model parameters that come from various measurements and has not a single variable adjusted to match the experimental results better. Thus, an asymmetric swimmer is much more adequate to reproduce the "wall-hugging" observed for real *Chlamydomonas* cells, when just considering steric interactions. The two sphere model has a clear physical motivation, by just considering wall induced torque because of the swimmers shape asymmetry as the only reorientation mechanism at the wall, as opposed to the model in [25] that produces similar results, but puts a direct curvature dependence into the equations of motion. The model simulated here simply produces the curvature dependence from the swimmers asymmetric shape. All in all, the model does not consider any hydrodynamic effects at all. Hydrodynamic interactions are commonly considered for the interactions of such microswimmers with walls [12, 24, 26] but

nevertheless we obtain good agreement with the experimental results, even without adjusting any parameters at all. The results of the performed simulations suggest not only a curvature guidance of these microalgae in confinement [11] (by changing the swimmers chance to escape a wall) but additionally a guidance due to curvature gradients, by influencing the orientation of the swimmer. Future experiments will explore the presence of this mechanism, but it does not seem unlikely considering the agreement in probability distribution.

4.1 Limits of the model

With the simplicity of the model there are some limitations that one has to keep in mind while studying it. The first is, of course, the fact that the model was until now only tested in quasi two-dimensional confinement, meaning that simulations were run in a 2d environment and experiments were carried out in confinements so strong that the swimmer could barely move up and down. Although simulations should be easily extendable to three-dimensional space, it remains unclear if two spheres are the right shape two choose in this case, since flagella probably do not draw a perfect 3d sphere while beating. Additionally the model has so far only been tested in strong confinement. How well predictions hold for less confining geometries is still to be tested.

The results of the simulations, when compared to experiments, give confidence that swimmer-wall interactions in strong confinement, similar to the natural habitat of *Chlamydomonas reinhardtii* as a soil-dwelling algae, can be reasonably well explained as due to steric interactions with the confining surface, and not due to hydrodynamics. Behavior of multiple cells may be different, with hydrodynamic interactions playing a bigger role there.

4.2 Outlook

Since *Chlamydomonas reinhardtii* as soil-dwelling algae are mostly found in geometrical environments much more complex than just circles or ellipses, the simulation code has been further modified to handle other geometrical shapes as well. Some of the images for the relative probability density, the time averaged orientation and the resulting rotation are shown in figure 21. They show even more pronounced vortices than in the elliptical compartments considered above. The figures shown here serve as an outlook to what potentially else can be done in the future and give a bit of an intuition of how *Chlamydomonas reinhardtii* may behave in more complex environments.

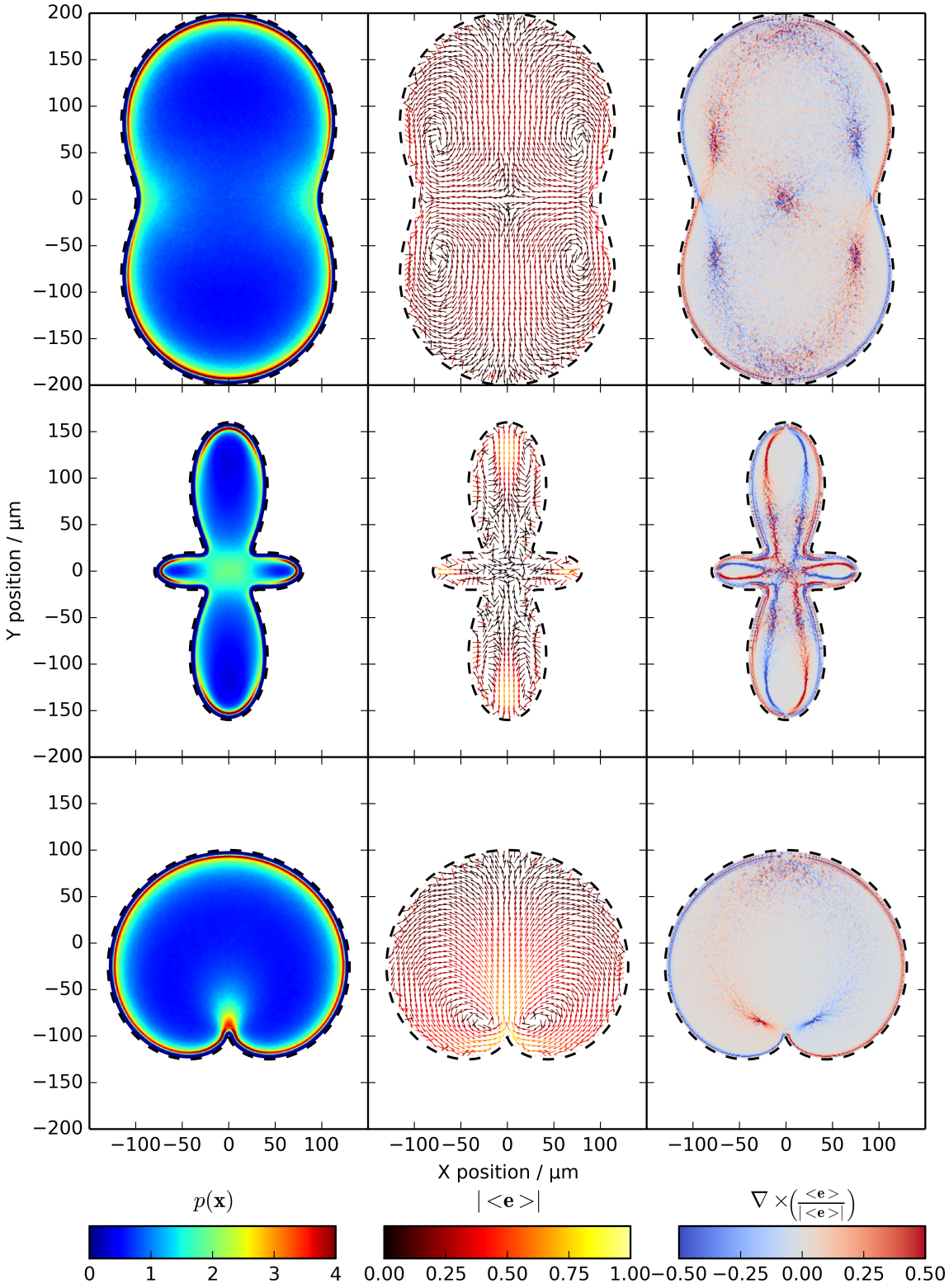

Figure 21: Relative probability density, average orientation vector field and its rotation for simulations in compartments of various shapes. It can be observed, that the swimmer barely stays at convex interfaces and that shapes with even higher gradients of curvature seem to produce even more probability flux.

In the future, the curvature gradient dependency may be studied with a focus on not only describing the effect qualitatively but on developing methods to quantify it better than just by visualizing the orientation vector field. Investigating how the model behaves with extreme gradients in curvature and extreme values of curvature up to confinements with sharp edges may give better insight on these effects as well. Expanding the model to three dimensions would also be interesting, especially investigating how the swimmer behaves on three dimensional walls with varying curvature.

Another point of interest would be to test if the predictions of the model hold true for other swimmers. A good starting point would be modeling *Chlamydomonas* mutants with different flagella length, but maybe even different microswimmer species employing similar propulsion techniques.

A Materials and Methods

A.1 Trigonometric identities

For $\varphi \in (-\pi, \pi)$ the following identity holds true [27]:

$$\tan\frac{\varphi}{2} = \sqrt{\frac{1-\cos\varphi}{1+\cos\varphi}} = \frac{\sin\varphi}{1+\cos\varphi}. \tag{A.1}$$

Now applying the transformation $\xi = \tan(\varphi/2)$ from section 2.3.2.1 gives

$$\begin{aligned} & \xi^2 = \frac{1-\cos\varphi}{1+\cos\varphi} \\ \Leftrightarrow \quad & \xi^2 = 1 - (\xi^2 - 1)\cos\varphi \\ \Leftrightarrow \quad & \cos\varphi = \frac{1-\xi^2}{1+\xi^2}, \end{aligned} \tag{A.2}$$

which is the first identity used in section 2.3.2.1. Then using the second equality from (A.1) and plugging in (A.2) leads to the second identity that is used:

$$\sin\varphi = \xi\left(1 + \frac{1-\xi^2}{1+\xi^2}\right) = \frac{2\xi}{1+\xi^2}. \tag{A.3}$$

A.2 Convex interfaces

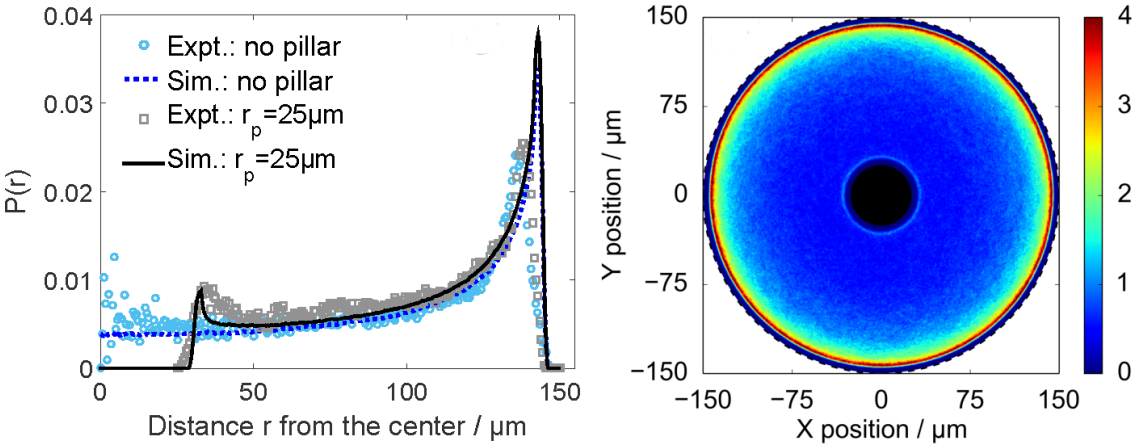

Figure A.1: Simulations and experiments were also carried out for circular compartments with a pillar in the middle. The swimmer spends much less time at convex interfaces. The left plot shows the radial probability distribution for experiments and simulations for circular compartments of $R = 150\mu$m with and without a pillar in the middle. The left plot shows the corresponding relative probability density for a simulation with pillar in the middle. Image adapted from [11].

A.3 Circular swimmer

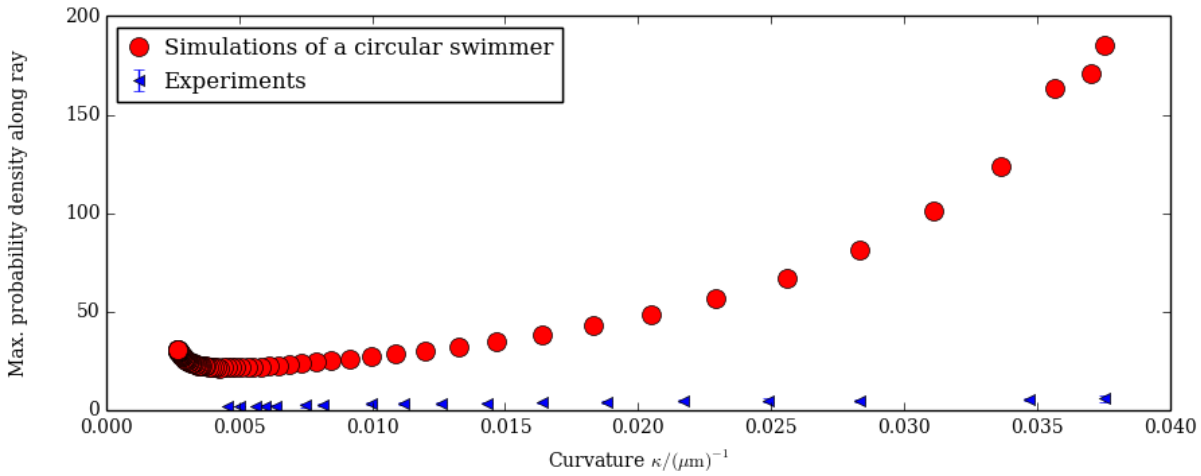

Figure A.2: The relative probability density peak height similar to figure 14, but with simulations for a circular swimmer. Simulations of a circular swimmer and experiments with *Chlamydomonas reinhardtii* [11] were carried out in an elliptical compartment of eccentricity $\varepsilon = 0.91$ and an area of $A_{\text{tot}} = 31316.7(\mu\text{m})^2$. A circular swimmer exhibits a much larger probability to be found at the wall, and a different dependence on curvature.

References

[1] A. Einstein, *Über die von der molekularkinetischen Theorie der Wärme geforderte Bewegung von in ruhenden Flüssigkeiten suspendierten Teilchen*, Annalen der Physik (1905).

[2] S. J. Ebbens and J. R. Howse, *In pursuit of propulsion at the nanoscale*, Soft Matter **6**, 726 (2010).

[3] W. C. K. Poon, *From Clarkia to Escherichia and Janus: the physics of natural and synthetic active colloids*, Proceedings of the International School of Physics Enrico Fermi", Course CLXXXIV "Physics of Complex Colloid", eds. C. Bechinger, F. Sciortino and P. Ziherl, IOS, Amsterdam: SIF, Bologna (2013).

[4] G. Volpe, S. Gigan, and G. Volpe, *Simulation of the active Brownian motion of a microswimmer*, American Journal of Physics **82**, 659 (2014).

[5] G. Gompper, *Microswimmers - from single particle motion to collective behaviour: lecture notes of the DFG SPP 1726 summer school 2015*, Forschungszentrum Jülich, Zentralbibliothek (2015).

[6] D. B. Weibel, P. Garstecki, D. Ryan, W. R. DiLuzio, M. Mayer, J. E. Seto, and G. M. Whitesides, *Microoxen: microorganisms to move microscale loads.*, Proceedings of the National Academy of Sciences of the United States of America **102**, 11963 (2005).

[7] J. R. Howse, R. A. L. Jones, A. J. Ryan, T. Gough, R. Vafabakhsh, and R. Golestanian, *Self-Motile Colloidal Particles: From Directed Propulsion to Random Walk*, Physical Review Letters **99**, 048102 (2007).

[8] U. Erdmann, W. Ebeling, L. Schimansky-Geier, and F. Schweitzer, *Brownian particles far from equilibrium*, European Physical Journal B: Condensed Matter and Complex Systems **15**, 105 (2000).

[9] J. Taktikos, *Modeling the random walk and chemotaxis of bacteria: Aspects of biofilm formation*, Universitätsbibliothek der Technischen Universität Berlin (2012).

[10] S. Merchant, *The Chlamydomonas genome reveals the evolution of key animal and plant functions*, Science **318**, 245 (2007).

[11] T. Ostapenko, F. Schwarzendahl, T. Böddeker, C. Kreis, J. Cammann, M. G. Mazza, and O. Bäumchen, *Curvature-guided motility of microalgae in geometric confinement*, Arxiv:1608.00363 (2016).

[12] E. Lauga and T. R. Powers, *The hydrodynamics of swimming microorganisms*, Reports on Progress in Physics **72**, 096601 (2009).

[13] A. Wysocki, J. Elgeti, and G. Gompper, *Giant adsorption of microswimmers: Duality of shape asymmetry and wall curvature*, Physical Review E **91**, 050302 (2015).

[14] E. M. Purcell, *Life at low Reynolds number*, American Journal of Physics **45**, 3 (1977).

[15] J. W. Shaevitz, J. Y. Lee, and D. A. Fletcher, *Spiroplasma swim by a processive change in body helicity*, Cell **122**, 941 (2005).

[16] I. Gibbons, *Cilia and flagella of eukaryotes*, The Journal of Cell Biology **91**, 107s (1981).

[17] H. C. Berg and R. a. Anderson, *Bacteria swim by rotating their flagellar filaments*, Nature **245**, 380 (1973).

[18] D. Bray, *Cell Movements: From molecules to motility*, Garland Science (2001).

[19] S. Kim and S. J. Karilla, *Microhydrodynamics: Principles and Selected Applications*, Butterworth-Heinemann (1991).

[20] G. G. Volpe, *Simulation of a Brownian particle in an optical trap*, American Journal of Physics **81**, 224 (2013).

[21] M. Polin, I. Tuval, K. Drescher, J. P. Gollub, and R. E. Goldstein, *Chlamydomonas swims with two "gears" in a eukaryotic version of run-and-tumble locomotion*, Science **325**, 487 (2009).

[22] V. Kantsler, J. Dunkel, M. Polin, and R. E. Goldstein, *Ciliary contact interactions dominate surface scattering of swimming eukaryotes*, Proceedings of the National Academy of Sciences of the United States of America **110**, 1187 (2013).

[23] P. E. Kloeden and E. Platen, *Numerical Solution of Stochastic Differential Equations*, Stochastics An International Journal of Probability and Stochastic Processes **23**, 1 (1992).

[24] E. Lushi, V. Kantsler, and R. E. Goldstein, *Scattering of bi-flagellate microswimmers from surfaces*, Arxiv:1608.02551 (2016).

[25] Y. Fily, A. Baskaran, and M. F. Hagan, *Dynamics of self-propelled particles under strong confinement*, Soft Matter **10**, 5609 (2014).

[26] K. Schaar, A. Zöttl, and H. Stark, *Detention times of microswimmers close to surfaces: Influence of hydrodynamic interactions and noise*, Physical Review Letters **115**, 038101 (2015).

[27] I. N. Bronstein, K. A. Semendjajew, G. Musiol, and H. Mühlig, *Taschenbuch der Mathematik*, vol. 23 (2008).

Erklärung nach §13(9) der Prüfungsordnung für den Bachelor-Studiengang Physik und den Master-Studiengang Physik an der Universität Göttingen:

Hiermit erkläre ich, dass ich diese Abschlussarbeit selbständig verfasst habe, keine anderen als die angegebenen Quellen und Hilfsmittel benutzt habe und alle Stellen, die wörtlich oder sinngemäß aus veröffentlichten Schriften entnommen wurden, als solche kenntlich gemacht habe.
Darüberhinaus erkläre ich, dass diese Abschlussarbeit nicht, auch nicht auszugsweise, im Rahmen einer nichtbestandenen Prüfung an dieser oder einer anderen Hochschule eingereicht wurde.

Göttingen, den 02. Dezember 2016

(Jan Cammann)